

Functional annotation of chemical libraries across diverse biological processes

Jeff S Piotrowski^{1,10,11}, Sheena C Li^{1,11} , Raamesh Deshpande^{2,11}, Scott W Simpkins^{3,11} , Justin Nelson³, Yoko Yashiroda¹, Jacqueline M Barber¹, Hamid Safizadeh^{2,4}, Erin Wilson², Hiroki Okada⁵, Abraham A Gebre⁵, Karen Kubo⁵, Nikko P Torres⁶, Marissa A LeBlanc¹, Kerry Andrusiak⁶, Reika Okamoto¹, Mami Yoshimura¹, Eva DeRango-Adem⁶, Jolanda van Leeuwen⁶ , Katsuhiko Shirahige⁷, Anastasia Baryshnikova^{8,10} , Grant W Brown^{6,9} , Hiroyuki Hirano¹, Michael Costanzo⁶ , Brenda Andrews⁶, Yoshikazu Ohya⁵, Hiroyuki Osada^{1*}, Minoru Yoshida^{1*}, Chad L Myers^{2,3*} & Charles Boone^{1,6*}

Chemical-genetic approaches offer the potential for unbiased functional annotation of chemical libraries. Mutations can alter the response of cells in the presence of a compound, revealing chemical-genetic interactions that can elucidate a compound's mode of action. We developed a highly parallel, unbiased yeast chemical-genetic screening system involving three key components. First, in a drug-sensitive genetic background, we constructed an optimized diagnostic mutant collection that is predictive for all major yeast biological processes. Second, we implemented a multiplexed (768-plex) barcode-sequencing protocol, enabling the assembly of thousands of chemical-genetic profiles. Finally, based on comparison of the chemical-genetic profiles with a compendium of genome-wide genetic interaction profiles, we predicted compound functionality. Applying this high-throughput approach, we screened seven different compound libraries and annotated their functional diversity. We further validated biological process predictions, prioritized a diverse set of compounds, and identified compounds that appear to have dual modes of action.

Discovery and development of novel compound libraries has outpaced the functional characterization of these compounds, leading to a growing knowledge gap¹. Chemical probes that target specific cellular functions are valuable entities, as they can provide insight into fundamental cellular functions and represent putative leads for new drug development. Despite a massive wealth of whole-genome sequence data that has identified hundreds of potential new druggable targets, in both humans and pathogens, we lack the chemical probes to take advantage of these insights². Therefore, a major demand exists for large-scale functional annotation of bioactive compounds.

Whole-cell screening approaches are advantageous because they identify bioavailable molecules and provide readouts based on general bioactivity³, a particular phenotypic response⁴, or a specific reporter system⁵ while maintaining biological context. Chemical genetics expands on traditional whole-cell screening, as it has the potential to monitor all cellular pathways in an unbiased manner⁶. A typical chemical-genetic screen involves testing a collection of mutant strains with defined genetic perturbations for fitness defects or advantages when grown in the presence of a specific compound^{6–8}. Quantifying the relative fitness of a collection of mutant strains in response to compound treatment generates a chemical-genetic

interaction profile, which provides diagnostic functional information about a compound's general mode of action^{7,9}.

Saccharomyces cerevisiae represents a powerful eukaryotic model system for chemical-genetic analysis because of its facile genetics and its available functional genomic reagents and tools. For example, genome-wide gene deletion analysis¹⁰ has identified ~1,000 essential genes and enabled the generation of a set of ~5,000 viable haploid deletion mutants. The essential genes can be exploited for chemical-genetic studies as heterozygous diploid mutants, whereas the nonessential genes can be studied as viable haploid deletion mutants such that each mutant is examined for hypersensitivity or resistance to a compound^{7,8}. Each strain is uniquely barcoded, allowing the responses of hundreds of pooled mutants to be measured simultaneously to generate a chemical-genetic interaction profile^{6,7}.

A comprehensive genetic interaction network, in which the majority of all possible double mutants are scored for genetic interactions quantitatively, has been mapped for yeast¹¹. A genetic interaction occurs when mutations in two or more genes combine to generate an unexpected phenotype. Given the single-mutant phenotypes, a negative genetic interaction occurs when two mutations combine to produce a double-mutant fitness defect that is more severe than

¹RIKEN Center for Sustainable Resource Science, Wako, Saitama, Japan. ²Department of Computer Science and Engineering, University of Minnesota-Twin Cities, Minneapolis, Minnesota, USA. ³Bioinformatics and Computational Biology Program, University of Minnesota-Twin Cities, Minneapolis, Minnesota, USA. ⁴Department of Electrical and Computer Engineering, University of Minnesota-Twin Cities, Minneapolis, Minnesota, USA. ⁵Department of Integrated Biosciences, Graduate School of Frontier Sciences, University of Tokyo, Kashiwa, Chiba, Japan. ⁶Donnelly Centre, University of Toronto, Toronto, Ontario, Canada. ⁷Institute of Molecular and Cellular Biosciences, Center for Epigenetic Disease, University of Tokyo, Bunkyo-ku, Tokyo, Japan. ⁸Lewis-Sigler Institute for Integrative Genomics, Princeton University, Princeton, New Jersey, USA. ⁹Department of Biochemistry, University of Toronto, Toronto, Ontario, Canada. ¹⁰Present addresses: Yumanity Therapeutics, Cambridge, Massachusetts, USA (J.S.P.); Calico Life Sciences, South San Francisco, California, USA (A.B.). ¹¹These authors contributed equally to this work. *e-mail: charlie.boone@utoronto.ca, chadm@umn.edu, hisyo@riken.jp or yoshidam@riken.jp

expected, whereas a positive genetic interaction reflects a double-mutant fitness defect that is less severe than expected. The set of negative and positive genetic interactions for a particular query gene represents a genetic interaction profile, which provides a quantitative description of gene function. A global network of genetic interaction profile similarities groups genes with similar roles into dense gene clusters representing major biological processes and thus highlights the functional organization of a cell^{11,12}. Importantly, a global compendium of genetic interaction profiles can be used to functionally interpret chemical-genetic interaction profiles^{9,12}. If a bioactive compound inhibits a specific target protein, then loss-of-function mutations in the corresponding target gene should mimic the bioactivity of the compound^{9,12}. Moreover, the genetic interaction profile of the target gene should resemble the chemical-genetic interaction profile of the inhibitory compound that modulates the target pathway^{9,12}. For example, the genetic interaction profile associated with a partial loss-of-function mutation in *ERG11*, which encodes the target of fluconazole, closely resembles the chemical-genetic interaction profile of fluconazole⁹. Thus, the global genetic interaction network provides a general key for interpreting the target pathways of bioactive compounds, enabling compounds to be annotated to specific biological processes and possibly specific pathways.

We developed a high-throughput chemical-genetic screening platform to functionally annotate large compound collections in a rapid and systematic manner. To do so, we constructed a diagnostic set of viable yeast gene-deletion mutants that span all major biological processes, each carrying a unique DNA barcode identifier, within a drug-sensitized, genetic background. We also developed a highly multiplexed (768-plex) barcode-sequencing protocol, allowing us to generate rich chemical-genetic profiles for hundreds of compounds simultaneously. Finally, we assembled a computational platform for functionally annotating compounds to specific biological processes and pathways. Ultimately, we applied this chemical-genetic pipeline to annotate seven diverse libraries containing 13,524 compounds in an unbiased and systematic manner.

RESULTS

Overview of the screening platform

To design a pipeline for high-throughput chemical-genetic profiling and functional annotation of chemical libraries (Fig. 1a), we first selected an optimal set of diagnostic genes and constructed a mutant strain collection in which each diagnostic gene was individually deleted in a drug-hypersensitive genetic background. Second, we developed a highly multiplexed barcode-sequencing¹³ system to enable chemical-genetic profiling with optimized signal detection. Third, we implemented computational approaches to integrate chemical-genetic profiles with the global yeast genetic interaction network to predict biological processes targeted by specific compounds. Finally, we assembled a database of chemical structures, chemical-genetic profiles, and functional predictions for each library investigated in this study.

A diagnostic gene set for chemical-genetic profiling

To increase the potential to detect bioactive compounds, we constructed a drug-sensitized yeast genetic background by combining deletions of *PDR1* and *PDR3*, both of which encode transcription factors known to regulate the yeast pleiotropic drug response¹⁴, with a deletion of *SNQ2*, which encodes a multidrug transporter (Supplementary Results, Supplementary Fig. 1). We tested growth of the resultant *pdr1Δ pdr3Δ snq2Δ* (3Δ) drug-sensitized strain in the presence of 440 different control compounds (see Online Methods; Supplementary Data Set 1), and observed a ~5-fold increase in the number of compounds that inhibited growth of the drug-sensitized strain compared to wild-type cells via a halo assay, indicating that these deletion mutations sensitized yeast to diverse classes of compounds (Fig. 1b)¹⁵. When considering the complete set of 13,524

compounds tested in this study, the average ‘hit rate’, corresponding to the fraction of bioactive compounds within a collection that causes at least 20% growth inhibition in the drug-sensitized strain in liquid medium, was ~35% across all compounds tested, which is ~5× greater than the hit rate found using the equivalent wild-type strain background in previous studies⁸ (Supplementary Data Set 1). Specific chemical-genetic interactions were also detected more readily in the drug-sensitized background. For example, at a concentration of 34.4 μM, the microtubule-binding compound benomyl showed a specific chemical-genetic interaction with *TUB3*, which encodes α-tubulin, only in our drug-sensitized background (Fig. 1c). Similarly, we analyzed the response to a cell wall β-1,3 glucan synthase inhibitor, micafungin, at 25 nM, and detected a specific chemical-genetic interaction with *BCK1*, which encodes a component of the protein kinase C (PKC) cell wall integrity signaling pathway (Fig. 1d). In both cases, only the known sensitive mutant showed an exaggerated chemical-genetic interaction, suggesting that, as in wild-type cells, the drug-sensitive background identifies functionally relevant signals (Fig. 1c,d).

Because genes within the same pathway and with the same biological process tend to share similar genetic interaction profiles^{9,12}, only a subset of genes are required to capture functionally informative genetic interaction signatures for a given gene. Leveraging this property, we developed a computational approach for optimal selection of mutants for chemical-genetic screens, identifying a set of 157 functionally diagnostic strains (Fig. 1e; see Online Methods). Independently, we also manually selected 236 strains mutated for genes spanning major yeast biological processes that belong to highly connected clusters in the global genetic interaction profile similarity network¹², 83 of which overlapped with the computationally selected set. Thus, the final diagnostic pool consisted of 310 deletion mutant strains (~6% of all nonessential genes) and spanned a similar functional space as the entire nonessential deletion mutant collection (Supplementary Fig. 2; Supplementary Data Set 2). Although members of our diagnostic subset are not distributed proportionally across the 17 major bioprocesses, these were selected not only for bioprocess representation but also for their predictive power (see Online Methods). Even though we are using a subset of strains, this diagnostic collection has been optimized for gene-similarity-based target prediction across the entire set of genetic interaction query strains (Fig. 1e).

Furthermore, we compared the individual fitness of each drug-sensitized deletion strain to that of its nonsensitized counterpart from the original deletion collection (Supplementary Data Set 2), and used this fitness score to select pool members with near-equivalent fitness. We observed that ~20% of the mutants in the diagnostic pool version 2.0 could not be scored by our standard synthetic genetic array (SGA) analysis scoring method because of irregularities in colony shape in the *pdr1Δ pdr3Δ snq2Δ* genetic background (Supplementary Data Set 2), and we verified that these mutants had appropriate fitness values based on barcode representation after pooled-liquid growth. Reducing the complexity of the collection of ~5,000 viable yeast deletion mutants to a smaller diagnostic set allowed us to maximize the dynamic range for detecting chemical-genetic interactions in a microculture and increased the degree of multiplexing for our barcode-sequencing readout.

Optimizing signal detection and high-throughput screening

Detecting drug–gene interactions requires a clear separation of sensitive and resistant mutants from the unaffected mutants in the pooled assay. To optimize signal detection, we tested the effects of three factors on detection of drug–gene interactions, using the well-characterized compounds benomyl and micafungin. The factors considered were inoculum size, incubation time, and the number of PCR cycles used for barcode DNA amplification (see Online Methods). Incubation time had the most pronounced

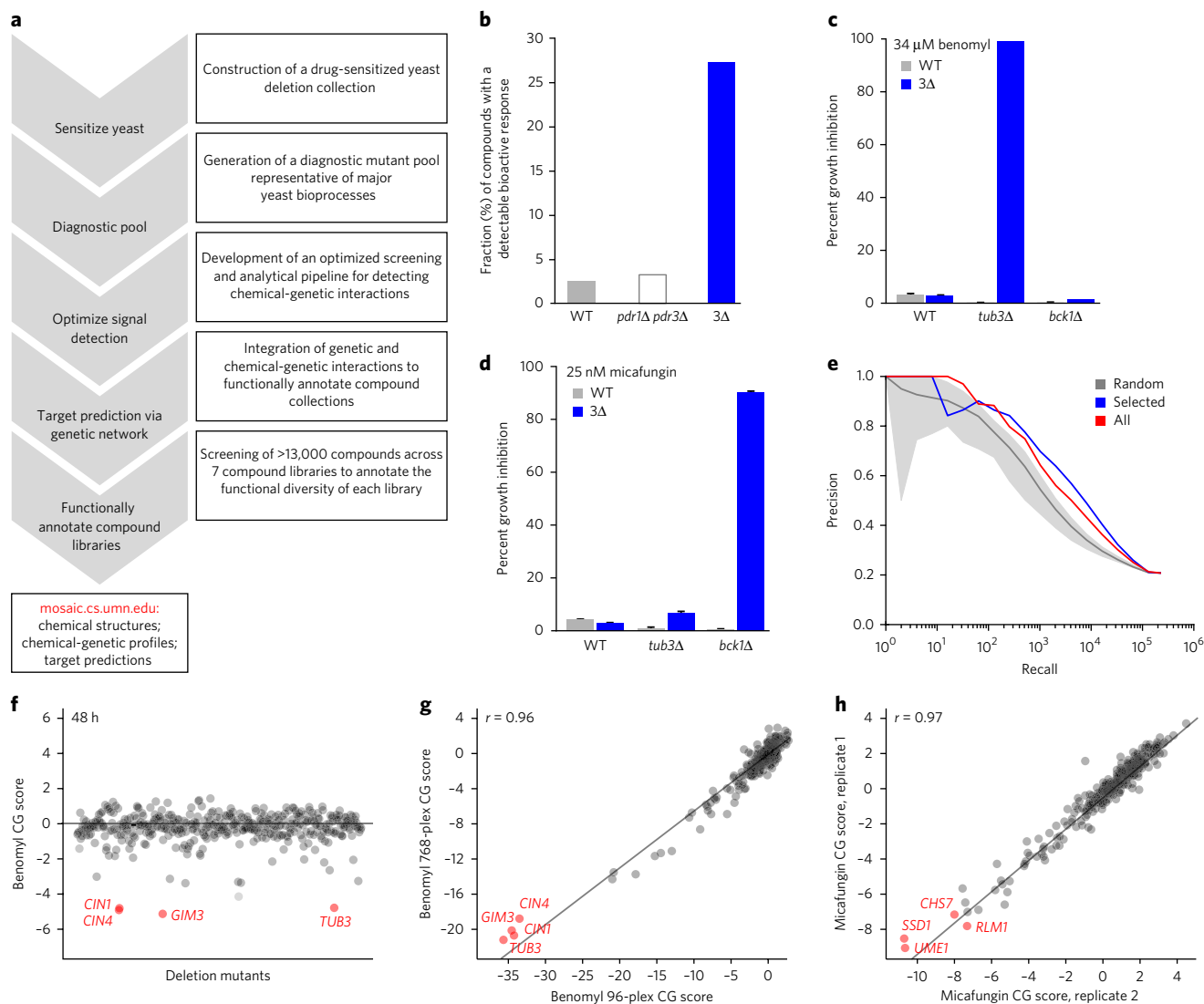


Figure 1 | Miniaturizing chemical-genetic profiling. (a) A high-throughput chemical-genetics platform for functional annotation of compound libraries. (b) The fraction (%) of compounds showing a bioactive response based on detection of a halo of growth inhibition surrounding a compound spotted on a lawn of WT strain, a *pdr1Δ pdr3Δ* double-mutant, or a *pdr1Δ pdr3Δ snq2Δ* triple-mutant strain (3Δ). (c) Comparison of WT and 3Δ strains in detecting a benomyl-*TUB3* chemical-genetic interaction ($n = 3$; experimental replicates mean \pm s.e.m.). (d) Comparison of WT and 3Δ strains in detecting a micafungin-*BCK1* chemical-genetic interaction ($n = 3$; mean \pm s.e.m.). (e) Plots of precision (true positives / (true positives + false positives)) versus recall (total number of true positives) to evaluate gene function predictions based on genetic interaction profile similarities derived from the entire nonessential deletion mutant collection (red), the diagnostic strain collection (blue), and a random selection of deletion strains the same size as the diagnostic collection (gray). True positives were defined as those gene pairs in which both genes are annotated to the same GO gold standard set of terms⁵⁰. (f) Detection of chemical-genetic interactions (red) following 48 h growth in the presence of benomyl. (g) Correlation (r) of average benomyl chemical-genetic interaction profiles ($n = 3$; technical replicates) derived from multiplexing 96 compared to 768 chemical genetic screens in a single sequencing lane. Benomyl-specific chemical-genetic interactions are shown in red. (h) Correlation of micafungin chemical-genetic interaction profiles derived from two independent experimental replicates. Specific micafungin chemical-genetic interactions are shown in red.

effect on the signal-to-noise ratio of the chemical-genetic profiles, with the optimal outcome observed after 48 h incubation (Fig. 1f; Supplementary Fig. 3a). For example, gene-deletion mutants defective in microtubule functions, including *CIN1*, *CIN4*, *GIM3*, and *TUB3*, were depleted efficiently from the culture after 48 h growth in the presence of benomyl. The assay was relatively robust to inoculum density and number of PCR amplification cycles (Supplementary Fig. 3a). Ultimately, the screening conditions we selected were 200-μL microcultures grown for 48 h at an inoculum of 250 cells/strain and 30 PCR cycles for barcode amplification. These parameters resulted in high correlation between biological replicates (Supplementary Fig. 3b).

Multiplexing of chemical-genetic samples is critical for screening large chemical libraries composed of thousands of compounds. Employing a custom-designed set of 768 multiplex primers, each containing a unique 10-bp multiplex tag (Supplementary Data Set 3; see Online Methods), we found that combining the barcode DNA samples from these 768 different chemical-genetic experiments produced profiles of similar quality to profiles for the same set of compounds generated at 96-plex (Fig. 1g). Thus, we adopted a screening strategy with 768 samples per Illumina HiSeq sequencing lane, or 6,144 samples per flow cell. Under these conditions, biological replicates (independently grown cultures of the same strain pool) from different sequencing lanes exhibited highly reproducible

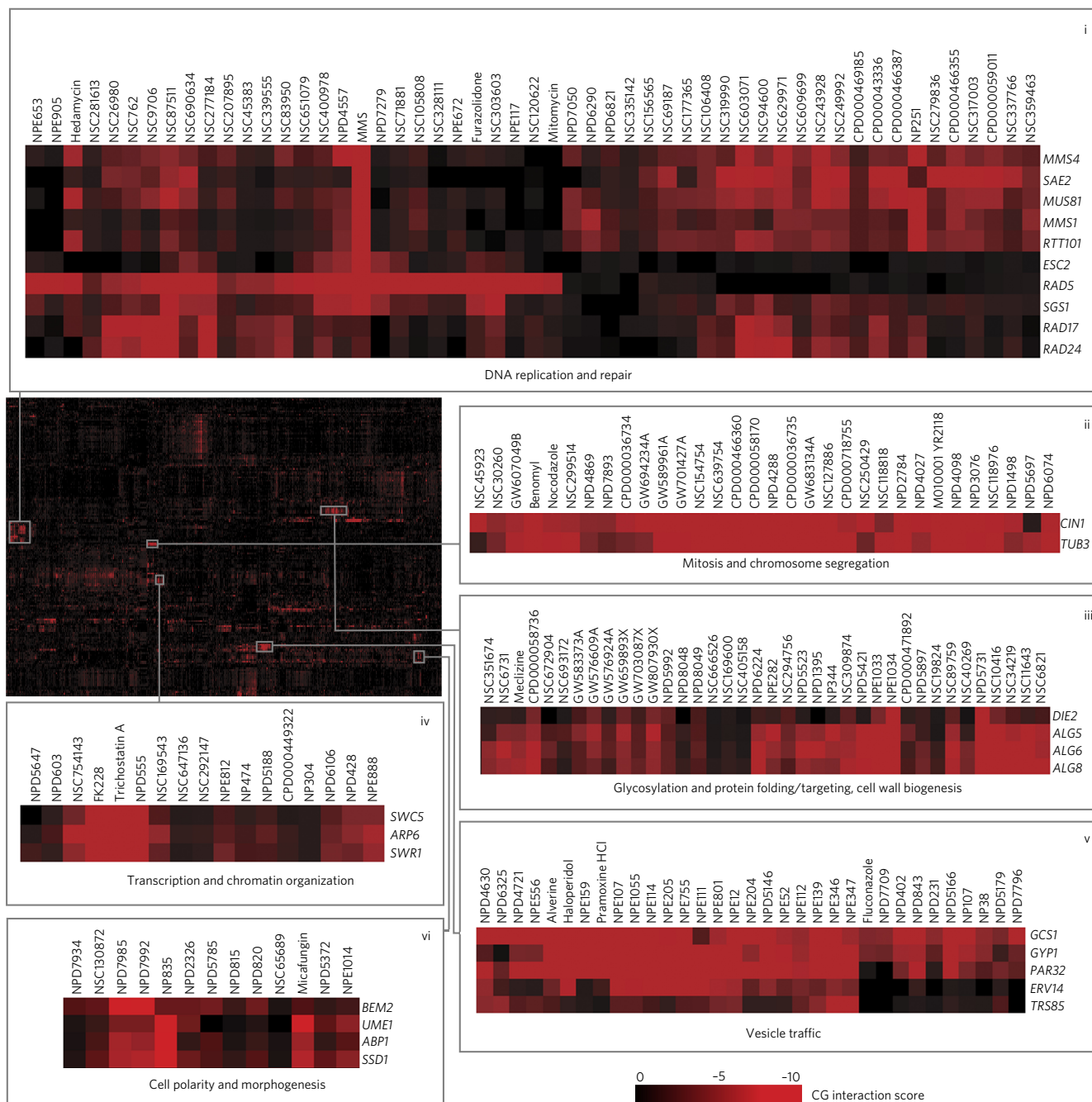


Figure 2 | Two-dimensional hierarchical clustering of chemical-genetic interactions. Mean negative chemical-genetic interactions are represented in red ($n = 3$, technical replicates). Rows, 177 deletion mutant strains; columns, 1,377 bioactive compounds from the high-confidence set (HCS). Sections are expanded to allow detailed visualization of compounds targeting processes related to DNA replication and repair (i); mitosis and chromosome segregation (ii); glycosylation, protein folding and targeting, and cell wall biogenesis (iii); transcription and chromatin organization (iv); vesicle traffic (v); and cell polarity and morphogenesis (vi).

chemical-genetic profiles (Fig. 1h). In pilot experiments, we sequenced barcodes using two separate reads, one for the multiplex tag and another for the deletion barcode; this methodology was thought to improve sequencing accuracy because it reduces the read length¹⁶. However, we achieved a more uniform distribution of sequence counts across conditions and barcoded mutants by using a single sequencing reaction designed to read through the entire PCR amplicon (Supplementary Fig. 3c).

Chemical-genetic profiling of diverse compound libraries

Applying our optimized pipeline, we generated chemical-genetic interaction profiles for 13,524 compounds by screening seven

diverse compound collections: the RIKEN Natural Product Depository (NPDepo), which is composed largely of purified natural products or natural product derivatives; four collections from the National Cancer Institute's Open Chemical Repository (natural products: NCI-NP; approved oncology drugs: NCI-ONC; structural and mechanistic diversity sets: NCI-STRUCT-DIV and NCI-MECH-DIV, respectively); a library of compounds from the National Institutes of Health Small Molecule Repository with a history of use in human clinical trials (NIH Clinical Collection or NIHCC); and the GlaxoSmithKline kinase inhibitor collection (GSK-KI). A complete description of these collections, all the compounds screened, their structures, their basic

physical properties, and the chemical-genetic data is provided (**Supplementary Data Sets 4–6**).

Chemical-genetic interactions were identified and scored by comparing the individual mutant barcode read counts to those from a set of solvent control conditions. A negative chemical-genetic (CG) interaction score represents hypersensitivity to a compound, whereas a positive CG score represents resistance (see Online Methods). At a relatively strict CG score threshold of ± 2.5 (z -score for enrichment or depletion in the presence of the compound relative to DMSO control), we observed positive chemical-genetic interactions between 0.5% of all compound–deletion–mutant pairs, and negative chemical-genetic interactions between 1.1% of all compound–deletion–mutant pairs. The set of highly bioactive compounds, which inhibited growth of the pooled collection by more than 20% (~4,700 compounds), exhibited a substantially higher frequency of chemical-genetic interactions, with positive and negative interactions occurring between 1.3% and 2.3% of compound–mutant pairs, respectively. Each deletion mutant displayed, on average, ~64 positive interactions and ~125 negative interactions across the entire collection of screened compounds. The number of chemical-genetic interactions for each strain (CG score ≥ 2.5 or ≤ -2.5) across all screened compounds is presented in **Supplementary Data Set 7**. Importantly, compounds screened both in our study, using the diagnostic set, and in previous studies, using the entire non-essential deletion mutant collection, showed positive correlations despite differences in strain backgrounds and methods used to measure mutant-strain abundance (microarray and sequencing) (**Supplementary Table 1**)^{8,17}.

Hierarchical clustering analysis^{7,9} provides a visual representation of the diversity of the resultant chemical-genetic profiles. We focused on the most responsive subset of 177 gene-deletion mutants, whose chemical-genetic profiles consisted of at least three extreme negative interactions (CG score ≤ -5), and 1,377 compounds derived from all seven collections (**Fig. 2**; See Online Methods). The clustered matrix highlighted chemical-genetic interactions involving sets of functionally related genes participating in different biological processes, including (i) DNA replication and repair; (ii) mitosis and chromosome segregation; (iii) glycosylation, protein folding and targeting, and cell wall biogenesis; (iv) transcription and chromatin organization; (v) vesicle traffic; (vi) cell polarity and morphogenesis; and other biological functions (**Fig. 2**). For example, a cluster of compounds, including benomyl and the tubulin-binding compound nocodazole, showed specific chemical-genetic interactions with *TUB3* and *CIN1*, suggesting that these compounds may target microtubule function or, more generally, target pathways with roles in mitosis and chromosome segregation. Indeed, this cluster includes a previously uncharacterized compound from the RIKEN NPDepto collection, NPD2784, which we found to strongly inhibit polymerization of mammalian tubulin *in vitro* (**Supplementary Fig. 4**).

Integrating genetic and chemical-genetic profiles

The chemical-genetic interaction profile of a compound that targets a specific biological process should overlap the genetic interaction profiles of genes that function as part of that process^{9,12}. To identify biological processes targeted by the compounds, we compared the chemical-genetic profile of each compound to our comprehensive set of genetic interaction profiles (**Supplementary Fig. 5**), allowing us to score each compound–gene pair for profile similarity (see Online Methods). This analysis generated a set of gene-level similarity scores, identifying a set of potential target genes for each compound. Although prediction of the precise gene target requires deeper experimental analysis, our approach was able to readily predict the biological process targeted by a particular compound based on Gene Ontology (GO) annotations shared among the target gene set (see Online Methods). To focus on high-confidence predictions,

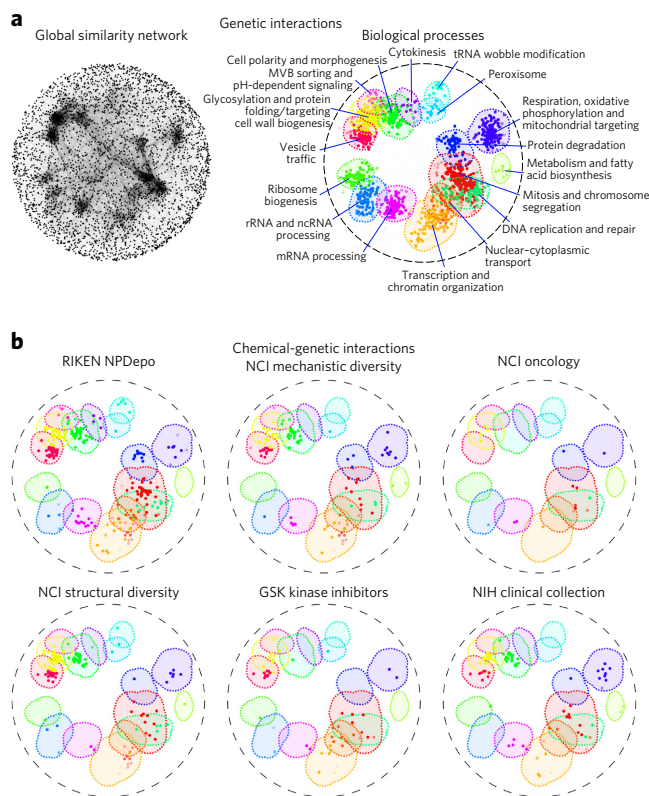


Figure 3 | The functional landscape of diverse compound collections.

(**a**) The global genetic interaction similarity network. Left, genes (nodes) that share similar genetic interaction profiles are connected by an edge in the global genetic interaction similarity network. Genes sharing highly similar patterns of genetic interactions are proximal to each other; less similar genes are positioned further apart. Right, densely connected network clusters, color coded by functional enrichment annotations to 17 distinct biological processes. (**b**) Integrating genetic and chemical-genetic interaction profiles to predict biological processes targeted by HCS compounds. Colored nodes represent chemical compounds derived from the indicated collection in **a**. Each compound was placed on the map at the position of the gene with the most similar genetic interaction profile from the compound's top predicted target process.

we estimated false discovery rates (FDR) for biological-process-level predictions based on both resampled and DMSO-control profiles and applied specific FDR thresholds (RIKEN NPDepto screen: FDR $\leq 25\%$; NCI/NIH/GSK screen: FDR $\leq 27\%$; see Online Methods). This analysis yielded 1,522 high-confidence compound profiles, which we refer to as our high-confidence set (HCS; **Supplementary Data Set 8**). We found that strains with many chemical-genetic interactions were important for bioprocess-level predictions (**Supplementary Data Set 9**). Interestingly, and in accordance with recent findings regarding the differences in functional information encoded by negative compared to positive genetic interactions¹¹, we found that negative chemical-genetic interactions were the primary driver of genetic-interaction-based target predictions, and without them, the quality of the predictions was reduced substantially (see Online Methods; **Supplementary Data Set 10**).

In general, we found that compound bioactivity was correlated with our ability to make high-confidence predictions, as ~82% of compounds in our high-confidence set inhibited growth >20% (**Supplementary Fig. 6**). However, the remaining ~18% of HCS compounds were associated with a more modest bioactivity (<20% growth inhibition), suggesting that even weakly bioactive compounds can yield functionally informative chemical-genetic profiles

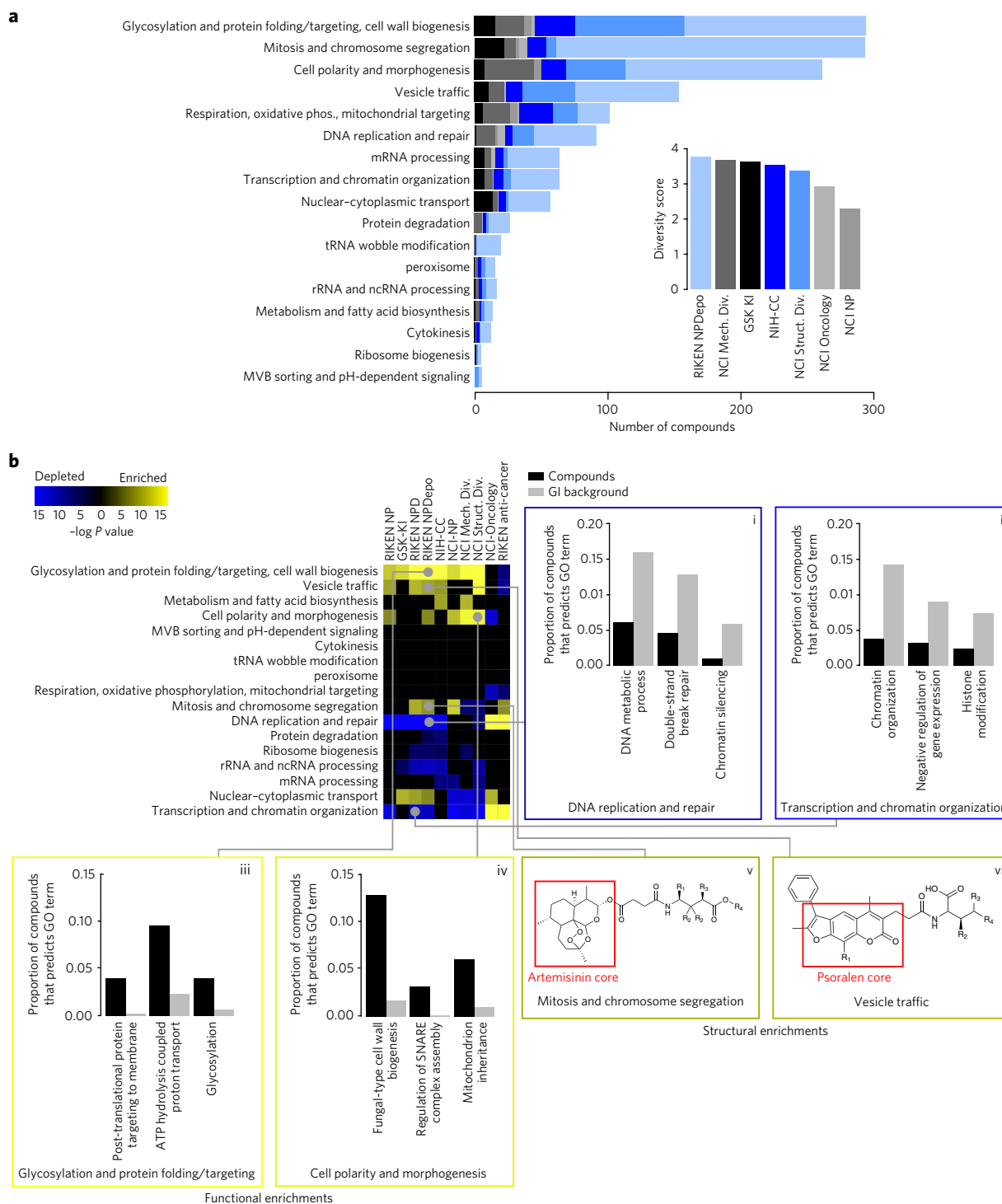


Figure 4 | Functional signatures of compound collections. (a) Number of compounds within each collection's HCS annotated to 17 distinct biological processes. Inset, estimated functional diversity of each collection based on the uniqueness of chemical-genetic profiles from each library. (b) Compound collections and subcollections were clustered based on their functional profiles. Collections whose chemical-genetic interaction profiles are enriched (yellow) or depleted (blue) for 17 distinct biological processes are shown. Sections are expanded (i-iv) to allow detailed visualization of the individual GO biological process annotations whose enrichments or depletions are summarized across 17 distinct bioprocesses. Black bars represent the proportion of compounds within a collection annotated to a GO biological process, and gray bars represent the proportion of profiles in the GI background set annotated to the same GO term. Enriched scaffold of artemisinin (v) and psoralen (vi) derivatives that are annotated to specific biological processes are shown. R groups of artemisinin derivative annotated to mitosis and chromosome segregation: NPD2911: R1 = R4 = H, R2 = Me, R3 = OH; NPD3902 R1 = R2 = R3 = R4 = H; NPD4196: R1 = R2 = R3 = H, R4 = succinimide; NPD7699 R1 = COOH, R2 = R3 = R4 = H). R groups of psoralen derivatives compounds annotated to vesicle traffic: NPD2851: R1 = R2 = R4 = Me, R3 = H; NPD3399: R1 = R3 = H, R2 = R4 = Me; NPD3811 R1 = R3 = R4 = Me, R2 = H; NPD3934: R1 = Me, R2 = R3 = R4 = H.

and that pre-screening for bioactivity may exclude some predictive profiles. A set of 296 compounds displayed extremely high bioactivity, with >90% growth inhibition, and nearly 60% (122) of these compounds were excluded from the final data set because their interaction profiles did not meet thresholds for strain representation. Interestingly, chemical-genetic profiles for these highly bioactive compounds showed that mutants defective for two genes involved in amino acid transport, *GTR1* and *AVT5*, were highly resistant and accounted for a majority of the read counts from these compound conditions. This suggests that these genes may play general roles in small-molecule transport and that their deletions may confer general resistance to highly bioactive compounds (Supplementary Fig. 7). We confirmed this finding for *gtr1Δ* cells in an independent experiment involving 23 different compounds (Supplementary Data Set 11).

Defining the functional landscape of compound collections

To view the functional diversity of entire compound collections, each HCS compound was mapped onto the global genetic interaction profile similarity network at the location of the gene that had the most similar genetic interaction profile to the compound's top predicted biological process target^{12,18}. The global network of genetic interaction profile similarities consists of 17 densely connected gene clusters, each representing a distinct biological process¹¹ (Fig. 3a). The integration of the set of chemical-genetic profiles from a particular compound collection into the global genetic interaction profile similarity network allowed visualization of functional space covered by the compound collection (Fig. 3b) and enabled quantification of the diversity of targeted biological processes (Fig. 4a).

Every major functional cluster in the genetic network appeared to be targeted by at least one compound screened in this study (Fig. 3b). However, glycosylation-, mitosis-, cell-polarity-, and vesicle-traffic-related functions were most frequently targeted, suggesting that these bioprocesses are more susceptible to chemical perturbation in yeast (Fig. 4a). When corrected for the number of compounds, the RIKEN NPDepo collection was the most functionally diverse collection, whereas the NCI natural products collection (Supplementary Fig. 8) was the least diverse. The NPDepo library can be partitioned chemically and mechanistically into different subset collections, including natural products (NP), natural product derivatives (NPD), and anticancer compounds (a manually curated list of RIKEN compounds with known anticancer activity; Supplementary Data Set 4), all of which showed distinct functional signatures in terms of their targeted bioprocess predictions. Each compound collection targets a unique set of biological processes (Figs. 3b and 4b), suggesting that this global view of collection functionality can aid prioritization of screening efforts based on specific bioprocess targets of interest.

For the larger collections, we observed compounds targeting all 17 biological processes represented in the global genetic interaction similarity map. For example, the RIKEN NPDepo library was large and diverse enough to target all the major biological processes (Fig. 4a,b). Interestingly, the rate at which compounds targeted different biological processes differed from the distribution of genes across bioprocesses, suggesting a biased chemical target space (Fig. 4b, i–iv). Although each chemical library displayed a unique set of predicted bioprocess targets, common signatures emerged across several of the collections. For example, we observed a ~4-fold enrichment of compounds targeting glycosylation- and protein-folding-related processes for most compound collections, including the NPDepo and NCI mechanistic diversity collections, the latter of which was designed to be relatively unbiased in terms of structure and functional annotations (Fig. 4b). Conversely, we saw a common depletion for compounds targeting DNA replication and repair- and transcription-related processes, suggesting that these processes are perturbed by compounds less frequently

than expected, which could be an important consideration in cases where, for example, targeting these biological processes for cancer therapeutics is a major goal.

Though enrichment for cytosolic and cell-surface targets and depletion for nuclear targets appeared as a general trend across several compound collections, exceptions were observed within specific libraries. In particular, for the NCI oncology collection, which is made up of anticancer agents largely directed toward the inhibition of cell division cycle functions and DNA replication and repair, we observed a strong enrichment for compounds targeting DNA replication and repair, and transcription and chromatin organization, relative to the expected background (Fig. 4b; $P < 0.001$). The NCI oncology collection, along with the anticancer subset of the RIKEN collection, differed the most from the general trend observed for larger, less-biased collections, reflecting the fact that these compounds have been selected for very specific purposes, largely confined to inhibiting growth of replicating cells.

The NIH-CC had a unique enrichment for compounds targeting metabolism and fatty acid biosynthesis, driven by GO predictions for sterol metabolic processes (Fig. 4b; Supplementary Data Set 12). The majority of these compounds interact with cytochrome P450 enzymes^{19–23}. In humans, compounds that inhibit or interact with cytochrome P450 have a high degree of drug–drug interactions²⁴. In yeast, cytochrome P450 homologs are ergosterol biosynthesis genes (*ERG11*, *ERG5*, and *NCPI*). Thus, the yeast system provides a means of predicting compounds that interact with human cytochrome P450 enzymes, possibly indicating compounds with a high degree of drug interactions.

The GSK kinase inhibitor (KI) library contains a characterized set of inhibitors of human kinases²⁵. Three compounds from this collection were previously identified to bind human mitogen- and stress-activated kinases (MSK)²⁶, and, in yeast, these had significant ($P < 0.05$) predictions for the GO process of intracellular protein-kinase cascade. This signaling pathway in yeast is mediated by the yeast mitogen-activated protein kinase encoded by *SLT2*, the top single-gene target prediction for all three compounds (Supplementary Data Set 13), and has high homology to human ERK1, ERK 2, and ERK 4. Furthermore, five compounds known to target human Polo-like kinase (PLK), were predicted in yeast to target the GO process protein targeting to the nuclear inner membrane (Supplementary Data Set 13). The yeast homolog of PLK is *CDC5*, which is involved in regulating nuclear shape. These examples again suggest that our yeast assay could be used to predict potential chemical bioprobes in human cells.

In general, the chemical-genetic functional signatures we observed appeared to be related to cellular localization, as cytoplasmic or cell-surface-related bioprocesses were more readily perturbed, and thus enriched, across diverse chemical libraries ($P < 0.0001$), whereas nuclear processes were less susceptible to chemical perturbation, and compounds predicted to target these processes were depleted among many of the libraries tested ($P < 0.0001$) (Supplementary Data Set 14). This finding may suggest that, in general, bioactive compounds are less likely to reach the nucleus, whereas cell-surface and cytosolic targets may be more druggable. This is consistent with a previous study²⁷ reporting that out of 1,362 annotated drug targets with orthologs across 4 mammalian species, only 8.4% of these targets localized to the nucleus, whereas 56% of targeted proteins localized to either membranes or the cytosol.

Integrating structural and functional data

As the RIKEN NPDepo contains sets of compound derivatives based upon variations of core scaffolds, we tested whether compounds predicted to target similar functions were enriched for specific structural classes (Fig. 4b, v–vi). Indeed, we found several instances in which a large class of structural derivatives had similar predicted modes of action (Supplementary Data Set 15). For example, chemical-genetic profile similarity grouped a coherent set

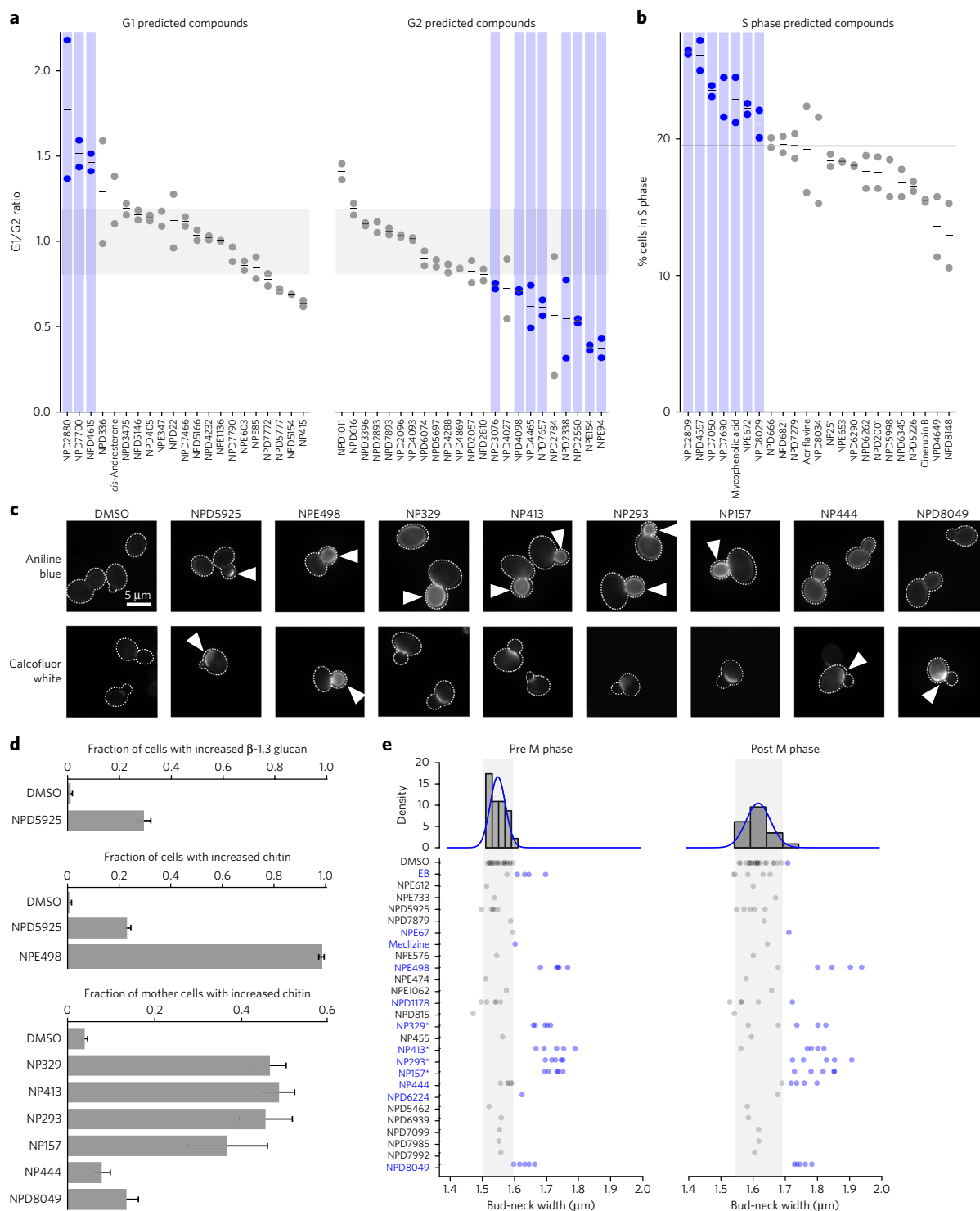


Figure 5 | Large-scale validation of predicted target processes. (a) Comparison of observed and predicted cell cycle arrest phenotypes induced by 67 high-confidence compounds. Observed phenotypes were derived from flow cytometry analysis and predicted phenotypes were generated by mapping biological process annotations of the 67 compounds from this study to cell cycle arrest phenotypes via ref. 35. Compounds that induced a G1 phase delay phenotype (G1/G2 ratio +1.5 s.d. from the DMSO mean—above the gray shaded box) or G2 phase delay phenotype (-1.5 s.d. from the DMSO mean—below gray shaded box) are indicated (blue circles, $n = 2$; experimental replicates). (b) Compounds confirmed by flow cytometry analysis to cause defects in S phase progression (at least 1.5 s.d. above the DMSO mean—above gray line) are indicated (blue circles, $n = 2$ biological replicates). (c) β -1,3 glucan (aniline blue) and chitin (calcofluor white) staining of cells treated with compounds predicted to affect the cell wall. Arrows indicate abnormal deposition of cell wall β -1,3 glucan or chitin. Scale bar, 5 μm . (d) Proportion of cells with increased β -1,3 glucan or chitin signal following treatment with predicted cell wall targeting compounds ($n = 3$; mean \pm s.e.m.). (e) Measurement of bud-neck width in pre- and post-M-phase cells following treatment with 25 compounds predicted to target the cell wall ($n \geq 2$; EB, echinocandin B). Blue text and circles indicate greater than average bud neck width. * denotes pseudojervine compounds.

of artemisinin derivatives (Fig. 4b, v) together within a broader subset of 358 compounds annotated to the ‘mitosis and chromosome segregation’ biological process. Although artemisinin is known to be an effective antimalarial drug, its cellular target(s) remain unclear²⁸. In yeast, artemisinin is known to affect functions of the cell cycle and mitochondria^{29,30}. Furthermore, artemisinin has well-established effects on cancer cell cycle progression^{31–33}. Our functional annotation supports both of these diverse roles for artemisinin, as our artemisinin-related natural product (NP266) was annotated with two different biological process predictions—mitochondrial cristae formation and microtubule cytoskeleton organization (Supplementary Data Set 8); however, the artemisinin derivatives that possess a relatively long side chain that extends from the three-ring core have stronger predictions for a mitosis-related rather than a mitochondrial bioprocess-level target.

In another example, the furanocoumarin tricycle (psoralen) structural class is represented by multiple derivatives within the NPDepo library (Fig. 4b, vi). Psoralen and its derivatives have been used to treat cutaneous T-cell carcinoma and dermatological conditions such as psoriasis and eczema³⁴. The RIKEN NPDepo psoralen derivatives were frequently predicted to affect vesicle trafficking and membrane-associated processes, and it is possible that other RIKEN NPDepo compounds with overlapping functional annotation could have similar therapeutic potential.

Targeted process validations and assessing predictive power

In a previous study, the DNA content of yeast mutant strains harboring conditional alleles of essential genes was analyzed by flow cytometry, showing how each essential gene affects cell cycle progression and mapping specific cell cycle progression defects to different biological processes³⁵. For example, inhibiting the function of essential genes involved in translation causes an accumulation of cells in G1 phase (‘G1’ phenotype), reflecting insufficient protein synthetic capacity to transit the restriction point in G1 (referred to as Start in yeast), whereas inhibiting genes involved in DNA synthesis causes a buildup of cells in S phase (‘S’ phenotype) and inhibiting mitosis genes results a G2 phase accumulation (‘G2’ phenotype). We performed high-throughput flow cytometry analysis on cell populations exposed to a set of 67 different HCS compounds from the RIKEN NPDepo (Supplementary Fig. 9) that were predicted to cause specific cell cycle arrest phenotypes (Fig. 5a,b). In total, 27 out of 67 (40%) of these compounds resulted in a cell cycle perturbation, and, overall, 19 out of 27 (70%) of compounds affecting cell cycle progression induced a phenotype consistent with our chemical-genetic predictions (Supplementary Data Set 16). For example, NPE94 was predicted to affect regulation of mitosis, and, indeed, cells treated with this compound accumulated in G2 phase (Fig. 5a). Compounds displaying a cell cycle phenotype showed significant enrichment for each of the compound’s predicted phenotypes over a background with permuted compound labels (G1: ~12-fold enrichment over background; $P < 0.001$; G2: ~3-fold enrichment; $P < 0.01$; S: 4-fold enrichment; $P < 0.001$) (Fig. 5a,b).

As a second validation, we examined the activity of 25 compounds annotated to cell-wall-related biological processes, using several different cell biological readouts. To serve as controls, we selected 24 high-confidence compounds with equivalent growth inhibition and diverse bioprocess-level predictions but excluding “cell polarity and morphogenesis” or “glycosylation, protein folding/targeting, and cell wall biosynthesis” bioprocess predictions (Supplementary Data Set 17). Microscopic examination of fluorescent staining of two different cell wall polymers, β -1,3 glucan and chitin, revealed that 8 of 25 (32%) cell-wall-predicted compounds induced abnormal cell-wall composition (Fig. 5c,d), and 11 of 25 (44%) caused increased bud-neck width (Fig. 5e), a common effect of cell-wall-targeting agents^{36,37}. Furthermore, seven of these compounds caused hypersensitivity

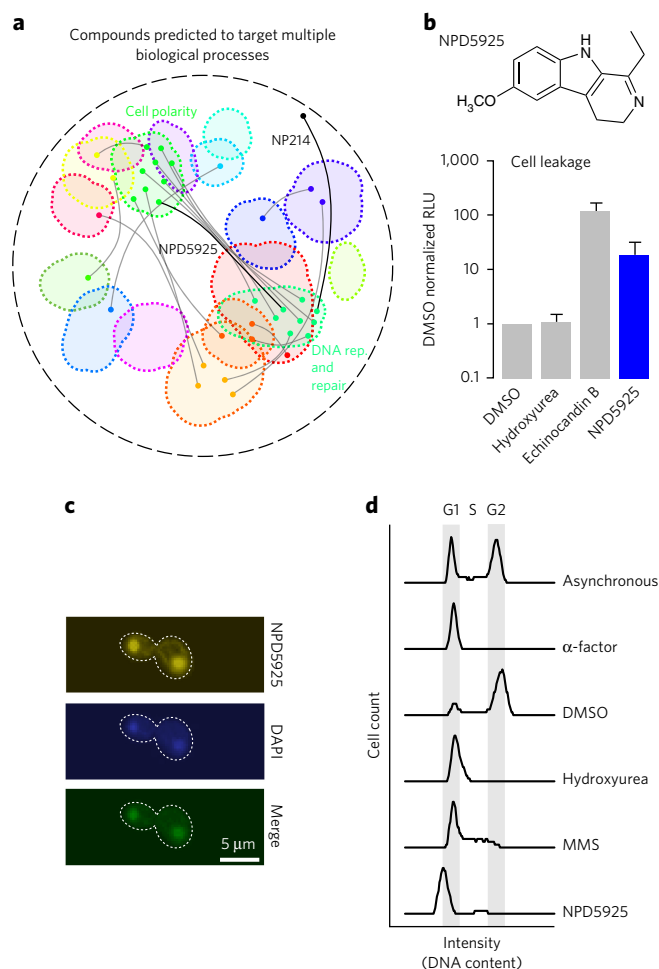


Figure 6 | Identification of compounds with dual targets. (a) Compounds predicted to target multiple distinct bioprocesses. Nodes indicate a predicted gene target located within a biological-process-enriched network cluster defined in the global genetic interaction profile similarity network. Edges represent compounds predicted to target two distinct biological processes. NPD5925 was predicted to target the distinct processes of DNA catabolic process and fungal-type cell wall biogenesis (yellow edge). NP214 was predicted to target DNA replication and cellular proton transport. (b) Measurement of cell leakage (adenylate kinase assay) from cells treated with DMSO, hydroxyurea, echinocandin B, and NPD5925 ($n = 3$ experimental replicates; mean \pm s.e.m.). (c) Images of a cell stained with NPD5925 (fluorescent), DAPI, and the merged fluorescent signal. Scale bar, 5 μ m. (d) Cell cycle analysis of cells following treatment with α -factor, DMSO, hydroxyurea (HU), MMS, and NPD5925.

to zymolyase (Supplementary Fig. 10a), which degrades yeast cell wall β -1,3 glucan. In addition, 3 of 25 compounds caused rapid cell leakage, similar to the effect with echinocandin B (Supplementary Fig. 10b), an antifungal drug that inhibits β -1,3 glucan biosynthesis. Among these compounds, we found a set of compounds that are structurally similar to pseudojervines (Supplementary Fig. 10c). Based on this, we predicted, and confirmed, that the poorly characterized parent compound jervine caused similar, abnormal glucan localization (Supplementary Fig. 10d). The proportion of compounds that showed cell wall phenotypes in the cell wall-predicted set of compounds was significantly greater than that in the control compounds, even when all pseudojervines were treated as one compound. Overall, 48% (12 of 25) of the compounds predicted to target cell-wall biosynthesis exhibited at least one cell-wall-defect-associated phenotype, and 36% (9 of 25) of the compounds exhibited at least

two such phenotypes (Supplementary Data Set 17). In contrast, only 4% (1 of 24) of the control compounds showed any defects in β -1,3 glucan or chitin staining ($P < 0.05$) (Supplementary Data Set 17).

Predicting compounds with dual targets

Our database of biological-process-level annotation also offers the potential to screen for compounds that have multiple targets. Many pharmaceuticals perturb multiple cellular functions³⁸, and identifying multifunctional compounds provides opportunities for drug repurposing and addressing potential side effects of clinical agents³⁹. We mined our HCS predictions to identify compounds that were associated with two distinct biological processes (Fig. 6a; Supplementary Table 2). One of the top-ranked compounds predicted to have multiple targets was NP214, a bleomycin A2 derivative. NP214 was predicted to target two different processes: (1) DNA replication ($P < 0.001$) and (2) cellular proton transport ($P < 0.0001$). The primary target of bleomycin and related compounds is DNA⁴⁰; however, there is also evidence suggesting that these compounds perturb cellular membranes^{41–43} via a secondary mode of action that could underlie bleomycin-induced side effect of lung fibrosis⁴¹. In mammalian cells, apart from its DNA activity, bleomycin has been shown to affect membrane redox potential and proton movement⁴⁴. Moreover, bleomycin–iron complexes generate singlet oxygen and cause lipid peroxidation^{45,46}. Thus, our chemical-genetic biological process predictions captured both the primary role of bleomycin (DNA damage) and secondary mechanisms that are consistent with known bleomycin side effects.

From a ranked list of predictions of dual targets (Supplementary Table 2) for HCS compounds, we observed a common coupling of DNA-related processes and cell-wall biogenesis (Fig. 6a). For example, when we exposed yeast cells to NPD5925, a new RIKEN NPDepo compound that was predicted to affect both DNA catabolism ($P < 0.001$) and cell-wall biogenesis ($P < 0.001$), they displayed cell-surface defects, such as zymolyase sensitivity (Supplementary Fig. 10) and a cell leakage phenotype resembling that of echinocandin B (Fig. 6b). Because NPD5925 is fluorescent, we imaged its staining pattern and found that it localized to the nucleus, similarly to DAPI (4',6-diamidino-2-phenylindole; Fig. 6c; Supplementary Fig. 11); it also induced a G1/early S phase cell cycle arrest, similar to the arrest observed with high levels of hydroxyurea (Fig. 6d)⁴⁷. Because a compound that targets a pleiotropic gene could appear to perturb multiple, unique processes, we scanned the global yeast genetic interaction network for examples of genes displaying this type of genetic interaction profile; however, we were unable to find a single gene that could explain the dual bioprocess-level predictions of NPD5925 (Supplementary Fig. 12), providing further evidence that it perturbs both DNA-catabolism and cell-wall-biogenesis processes independently.

Despite the clear dual target signal of these compounds, the effect of dose likely plays a substantial role in separating the multiple modes of action of a compound. Indeed, a dose curve would likely help to further dissect primary from secondary mechanisms of action of compounds. For example, in the case of NP214 and NPD5925, it is possible that DNA may be the primary target, and thus the DNA binding CG score signal would likely be apparent at lower doses, whereas the cellular proton transport or cell-wall signals may only be detectable at higher doses. However, as we have screened dozens of DNA-damaging agents that have not yielded these specific dual-target signals, it is not likely that these findings are a consequence of general effects on DNA. While we still do not know the exact mechanism of NPD5925, we are able to deconstruct complex phenotypic consequences of a compound.

New chemical-genetic resources and analytical tools

We generated an active database named MOSAIC (<http://mosaic.cs.umn.edu/>), housing all our chemical-genetic screens. The MOSAIC

database catalogs the structural and basic physical properties of all compounds tested, including their bioactivity, chemical-genetic profiles, as well as the biological process and gene-level target predictions. We also developed novel software tools, called BEAN-counter (barcoded experiment analysis from next-generation sequencing), for processing raw sequencing data into chemical-genetic interaction profiles, and CG-TARGET (chemical-genetic translation via a reference genetic interaction network), for predicting biological-process-level targets from chemical-genetic interaction profiles. These new software tools are available at <http://github.com/csbio/>.

The bioprocess diversity set

We distilled the most functionally diverse compounds from all seven libraries analyzed in this study into a new 'bioprocess diversity set' (Supplementary Data Set 18), which represents a selected collection of our HCS bioactive compounds whose targets span the functional landscape of the cell. We also selected 'bioprocess specific sets', each consisting of a set of compounds predicted to target one of the 17 different biological processes represented in the global genetic-interaction profile similarity network (Supplementary Data Set 19). We anticipate that these new compound collections will provide a powerful new resource for modulating cellular physiology through diverse perturbations and streamlining of the chemical-genetic discovery pipeline, enabling a focused analysis on specific biological processes of interest. The bioprocess diversity set and the bioprocess specific sets can easily be sorted to focus on individual compound libraries, including the NCI, NIH, GSK, and RIKEN NPDepo libraries.

DISCUSSION

Our high-throughput chemical-genetics platform addresses a need for an unbiased, whole-cell method that provides rapid, functional annotation of compound libraries. We used this system to screen 13,524 compounds across 7 different libraries, yielding rich chemical-genetic profiles and high-confidence functional predictions for a set of 1,522 compounds. We cataloged the complete data set as an open chemical-genetics resource (<http://mosaic.cs.umn.edu/>).

Our functional annotation of chemical libraries offers a strategy for prioritizing compounds that display bioactivity directed toward particular biological processes. The scale of functional annotation also provides a global view of the chemical activity within a library, which should allow testing of general hypotheses relevant to chemical biology. Importantly, the high-throughput nature of this assay provides opportunities for systematic, large-scale functional analysis of natural extract collections. Natural extract collections are often far more expansive than pure compound libraries and may contain broader mechanistic diversity. Functional annotation of these collections would help identify and prioritize promising extracts for detailed fractionation⁷.

Our approach highlights the use of drug-sensitized and diagnostic mutant sets for compound characterization, which allowed us to interrogate more compounds and use smaller quantities. Certain drug efflux transporters can be dedicated to certain classes of drugs, such as *PDR5*, which has a documented specificity to steroid drugs⁴⁸. Thus, although we explored only one genetic background for sensitization, it is possible to construct new yeast mutant collections using different genetic backgrounds tailored specifically for hypersensitivity to particular drug classes. In addition, while we selected a diagnostic pool of mutants specifically for genome-wide functional annotation, diagnostic pools with specific functional biases could be designed to investigate particular cellular processes or targets. Moreover, the diagnostic pool may be further reduced in size for greater multiplexing, as we found that a set of as few as 157 strains had equivalent predictive power to the entire nonessential collection of 5000 strains.

One advantage of our approach is that we can functionally characterize compounds that do not show strong bioactivity. Although bioactivity was predictive of our ability to make high-confidence predictions, it was not absolutely necessary. Pre-screening for bioactivity, which is a common approach^{8,17}, can potentially exclude compounds with specific but possibly nonessential modes of action. For example, ~18% (270 of 1,518) of the HCS compounds with measured bioactivity inhibited growth <20%. Indeed, weakly acting compounds targeting specific functions represent a starting point for chemical modifications to improve bioactivity.

Biological-process target predictions derived from the global *S. cerevisiae* genetic interaction network provides a roadmap not only for other microorganisms (for example, *Schizosaccharomyces pombe* and *Escherichia coli*) but also for mammalian systems. Importantly, the construction of genetic interaction maps in human cell lines is possible, as is the mapping of chemical-genetic interactions⁴⁹. Thus, the same approaches and predictive tools we implemented in yeast can be adapted and applied as a general strategy to map analogous chemical-genetic networks for human cells. More generally, combinatorial genetic and chemical-genetic approaches can be used to identify new drug leads that work synergistically to expand our understanding of druggable target space.

Received 6 September 2016; accepted 13 June 2017;
published online 24 July 2017; corrected before print 7 August 2017 (details online)

METHODS

Methods, including statements of data availability and any associated accession codes and references, are available in the [online version of the paper](#).

References

- Geysen, H.M., Schoenen, F., Wagner, D. & Wagner, R. Combinatorial compound libraries for drug discovery: an ongoing challenge. *Nat. Rev. Drug Discov.* **2**, 222–230 (2003).
- Roemer, T. & Boone, C. Systems-level antimicrobial drug and drug synergy discovery. *Nat. Chem. Biol.* **9**, 222–231 (2013).
- Kepp, O., Galluzzi, L., Lipinski, M., Yuan, J. & Kroemer, G. Cell death assays for drug discovery. *Nat. Rev. Drug Discov.* **10**, 221–237 (2011).
- Clemons, P.A. Complex phenotypic assays in high-throughput screening. *Curr. Opin. Chem. Biol.* **8**, 334–338 (2004).
- Sundberg, S.A. High-throughput and ultra-high-throughput screening: solution- and cell-based approaches. *Curr. Opin. Biotechnol.* **11**, 47–53 (2000).
- Giaever, G. et al. Chemogenomic profiling: identifying the functional interactions of small molecules in yeast. *Proc. Natl. Acad. Sci. USA* **101**, 793–798 (2004).
- Parsons, A.B. et al. Exploring the mode-of-action of bioactive compounds by chemical-genetic profiling in yeast. *Cell* **126**, 611–625 (2006).
- Lee, A.Y. et al. Mapping the cellular response to small molecules using chemogenomic fitness signatures. *Science* **344**, 208–211 (2014).
- Parsons, A.B. et al. Integration of chemical-genetic and genetic interaction data links bioactive compounds to cellular target pathways. *Nat. Biotechnol.* **22**, 62–69 (2004).
- Giaever, G. et al. Functional profiling of the *Saccharomyces cerevisiae* genome. *Nature* **418**, 387–391 (2002).
- Costanzo, M. et al. A global genetic interaction network maps a wiring diagram of cellular function. *Science* **353**, aaf1420 (2016).
- Costanzo, M. et al. The genetic landscape of a cell. *Science* **327**, 425–431 (2010).
- Smith, A.M. et al. Highly-multiplexed barcode sequencing: an efficient method for parallel analysis of pooled samples. *Nucleic Acids Res.* **38**, e142 (2010).
- Rogers, B. et al. The pleiotropic drug ABC transporters from *Saccharomyces cerevisiae*. *J. Mol. Microbiol. Biotechnol.* **3**, 207–214 (2001).
- Andrusiak, K. *Adapting S. cerevisiae Chemical Genomics for Identifying the Modes of Action of Natural Compounds* (Master's thesis, University of Toronto, 2012).
- Bokulich, N.A. et al. Quality-filtering vastly improves diversity estimates from Illumina amplicon sequencing. *Nat. Methods* **10**, 57–59 (2013).
- Hoepfner, D. et al. High-resolution chemical dissection of a model eukaryote reveals targets, pathways and gene functions. *Microbiol. Res.* **169**, 107–120 (2014).
- Baryshnikova, A. Systematic functional annotation and visualization of biological networks. *Cell Syst.* **2**, 412–421 (2016).
- Vancutsem, P.M. & Babish, J.G. *In vitro* and *in vivo* study of the effects of enrofloxacin on hepatic cytochrome P-450. Potential for drug interactions. *Vet. Hum. Toxicol.* **38**, 254–259 (1996).
- Desta, Z., Soukhova, N., Mahal, S.K. & Flockhart, D.A. Interaction of cisapride with the human cytochrome P450 system: metabolism and inhibition studies. *Drug Metab. Dispos.* **28**, 789–800 (2000).
- Jeong, S., Nguyen, P.D. & Desta, Z. Comprehensive *in vitro* analysis of voriconazole inhibition of eight cytochrome P450 (CYP) enzymes: major effect on CYPs 2B6, 2C9, 2C19, and 3A. *Antimicrob. Agents Chemother.* **53**, 541–551 (2009).
- Abdel-Rahman, S.M. et al. Potent inhibition of cytochrome P-450 2D6-mediated dextromethorphan O-demethylation by terbinafine. *Drug Metab. Dispos.* **27**, 770–775 (1999).
- Laugesen, S., Enggaard, T.P., Pedersen, R.S., Sindrup, S.H. & Brøsen, K. Paroxetine, a cytochrome P450 2D6 inhibitor, diminishes the stereoselective O-demethylation and reduces the hypoalgesic effect of tramadol. *Clin. Pharmacol. Ther.* **77**, 312–323 (2005).
- Dresser, G.K., Spence, J.D. & Bailey, D.G. Pharmacokinetic-pharmacodynamic consequences and clinical relevance of cytochrome P450 3A4 inhibition. *Clin. Pharmacokinet.* **38**, 41–57 (2000).
- Dranchak, P. et al. Profile of the GSK published protein kinase inhibitor set across ATP-dependent and-independent luciferases: implications for reporter-gene assays. *PLoS One* **8**, e57888 (2013).
- Bamford, M.J. et al. (1H-imidazo[4,5-c]pyridin-2-yl)-1,2,5-oxadiazol-3-ylamine derivatives: a novel class of potent MSK-1-inhibitors. *Bioorg. Med. Chem. Lett.* **15**, 3402–3406 (2005).
- Wang, X., Wang, R., Zhang, Y. & Zhang, H. Evolutionary survey of druggable protein targets with respect to their subcellular localizations. *Genome Biol. Evol.* **5**, 1291–1297 (2013).
- O'Neill, P.M., Barton, V.E. & Ward, S.A. The molecular mechanism of action of artemisinin--the debate continues. *Molecules* **15**, 1705–1721 (2010).
- Li, W. et al. Yeast model uncovers dual roles of mitochondria in action of artemisinin. *PLoS Genet.* **1**, e36 (2005).
- Steinbrück, L., Pereira, G. & Efferth, T. Effects of artesunate on cytokinesis and G/M cell cycle progression of tumour cells and budding yeast. *Cancer Genomics Proteomics* **7**, 337–346 (2010).
- Disbrow, G.L. et al. Dihydroartemisinin is cytotoxic to papillomavirus-expressing epithelial cells in vitro and in vivo. *Cancer Res.* **65**, 10854–10861 (2005).
- Li, Y. et al. Novel antitumor artemisinin derivatives targeting G1 phase of the cell cycle. *Bioorg. Med. Chem. Lett.* **11**, 5–8 (2001).
- Goodrich, S.K., Schlegel, C.R., Wang, G. & Belinson, J.L. Use of artemisinin and its derivatives to treat HPV-infected/transformed cells and cervical cancer: a review. *Future Oncol.* **10**, 647–654 (2014).
- Xia, W. et al. Photo-activated psoralen binds the ErbB2 catalytic kinase domain, blocking ErbB2 signaling and triggering tumor cell apoptosis. *PLoS One* **9**, e88983 (2014).
- Yu, L., Peña Castillo, L., Mnaimneh, S., Hughes, T.R. & Brown, G.W. A survey of essential gene function in the yeast cell division cycle. *Mol. Biol. Cell* **17**, 4736–4747 (2006).
- Piotrowski, J.S. et al. Plant-derived antifungal agent poaic acid targets β -1,3-glucan. *Proc. Natl. Acad. Sci. USA* **112**, E1490–E1497 (2015).
- Okada, H., Ohnuki, S., Roncero, C., Konopka, J.B. & Ohya, Y. Distinct roles of cell wall biogenesis in yeast morphogenesis as revealed by multivariate analysis of high-dimensional morphometric data. *Mol. Biol. Cell* **25**, 222–233 (2014).
- Peters, J.-U., Schneider, P., Mattei, P. & Kansy, M. Pharmacological promiscuity: dependence on compound properties and target specificity in a set of recent Roche compounds. *ChemMedChem* **4**, 680–686 (2009).
- Medina-Franco, J.L., Giulianotti, M.A., Welmaker, G.S. & Houghten, R.A. Shifting from the single to the multitarget paradigm in drug discovery. *Drug Discov. Today* **18**, 495–501 (2013).
- Grollman, A.P. & Takeshita, M. Interactions of bleomycin with DNA. *Adv. Enzyme Regul.* **18**, 67–83 (1980).
- Hay, J., Shahzeidi, S. & Laurent, G. Mechanisms of bleomycin-induced lung damage. *Arch. Toxicol.* **65**, 81–94 (1991).
- Moore, C.W., Del Valle, R., McKoy, J., Pramanik, A. & Gordon, R.E. Lesions and preferential initial localization of [S-methyl-3H]bleomycin A2 on *Saccharomyces cerevisiae* cell walls and membranes. *Antimicrob. Agents Chemother.* **36**, 2497–2505 (1992).
- Poddevin, B., Orłowski, S., Belehradek, J. Jr. & Mir, L.M. Very high cytotoxicity of bleomycin introduced into the cytosol of cells in culture. *Biochem. Pharmacol.* **42**, (Suppl.), S67–S75 (1991).
- Sun, I.L. & Crane, F.L. Bleomycin control of transplasma membrane redox activity and proton movement in HeLa cells. *Biochem. Pharmacol.* **34**, 617–622 (1985).
- Ekimoto, H., Takahashi, K., Matsuda, A., Takita, T. & Umezawa, H. Lipid peroxidation by bleomycin-iron complexes in vitro. *J. Antibiot. (Tokyo)* **38**, 1077–1082 (1985).

46. Kanofsky, J.R. Singlet oxygen production by bleomycin. A comparison with heme-containing compounds. *J. Biol. Chem.* **261**, 13546–13550 (1986).
47. Sidorova, J.M. & Breeden, L.L. Precocious G1/S transitions and genomic instability: the origin connection. *Mutat. Res.* **532**, 5–19 (2003).
48. Mahé, Y., Lemoine, Y. & Kuchler, K. The ATP binding cassette transporters Pdr5 and Snq2 of *Saccharomyces cerevisiae* can mediate transport of steroids in vivo. *J. Biol. Chem.* **271**, 25167–25172 (1996).
49. Hart, T. *et al.* High-resolution CRISPR screens reveal fitness genes and genotype-specific cancer liabilities. *Cell* **163**, 1515–1526 (2015).
50. Myers, C.L., Barrett, D.R., Hibbs, M.A., Huttenhower, C. & Troyanskaya, O.G. Finding function: evaluation methods for functional genomic data. *BMC Genomics* **7**, 187 (2006).

Acknowledgments

This work was supported by RIKEN Strategic Programs for R&D. J.S.P. and S.C.L. were funded by a RIKEN Foreign Postdoctoral Fellowship. S.W.S. is supported by an NSF Graduate Research Fellowship (00039202), an NIH Biotechnology training grant (T32GM008347), and a one-year BICB fellowship from the University of Minnesota. H.O. is a research fellow of the Japan Society for the Promotion of Science (JSPS). R.D., J.N., E.W., and C.L.M. are supported by National Institutes of Health Grants 1R01HG005084-01A1, 1R01GM104975-01, and R01HG005853 and National Science Foundation Grant DBI 0953881. C.B. and Y.O. are supported by JSPS KAKENHI Grant Numbers 15H04483. C.B. and B.A. were supported by the Canadian Institutes of Health Research, grants FDN-143264 and FDN-143265, respectively. C.L.M., C.B., M.C., J.L., and B.A. are supported by the Canadian Institute for Advanced Research Genetic Networks Program. Y.O. is supported by Ministry of Education, Culture, Sports, Science and Technology, Japan Grant for Scientific Research 24370002 and JSPS KAKENHI Grant Numbers 15H04402. M. Yoshida is supported by JSPS KAKENHI Grant Number 26221204. A.B. is supported by a Lewis Sigler fellowship at Princeton University.

G.W.B. and N.P.T. are supported by Canadian Cancer Society Research Institute impact grant 702310. K.S. is supported by The Core Research for Evolutional Science and Technology (CREST) from the Japan Science and Technology Agency (JST). We thank Astellas Pharma, Inc. (Tokyo, Japan) for their kind gift of micafungin. We thank T. Saito for help with NPDepo compound access. Sequencing was provided by RIKEN Center for Life Science Technologies, Division of Genomic Technologies, Genome Network Analysis Support Facility (GeNAS) RIKEN CLST and the University of Chicago.

Author contributions

C.B., M. Yoshida, C.L.M., J.S.P. and S.C.L. conceived the project. J.S.P., S.C.L., R.D., and S.W.S. designed the chemical genomic screens. J.S.P., S.C.L., J.M.B., R.O., M. Yoshimura, Y.Y., E. D.-A. performed the chemical genomic experiments. C.L.M., R.D., S.W.S., J.N., H.S., and E.W. designed the analysis software and performed analysis. G.W.B., N.P.T., and S.C.L. performed cell cycle experiments. J.P., K.A., M.A.L., and A.B. designed the sensitized yeast. Y.O., H.O., A.A.G., K.K. performed validation of cell wall targeting compounds. R.D. and M.C. designed the diagnostic mutant collection. H.O. and H.H. provided and curated NPDepo compounds. K.S. and B.A. provided analysis. J.v.L. edited the figures of the manuscript. The manuscript was written by J.S.P., S.C.L., C.L.M., and C.B. with input and editing from all authors.

Competing financial interests

The authors declare no competing financial interests.

Additional information

Any supplementary information, chemical compound information and source data are available in the [online version of the paper](#). Reprints and permissions information is available online at <http://www.nature.com/reprints/index.html>. Publisher's note: Springer Nature remains neutral with regard to jurisdictional claims in published maps and institutional affiliations. Correspondence and requests for materials should be addressed to H.O., M. Yoshida, C.L.M. or C.B.

ONLINE METHODS

Constructing a genome-wide drug sensitive yeast deletion collection. Construction of the *ptr1Δ ptr3Δ snq2Δ* triple mutant was carried out as previously described¹⁵. Briefly, *PDR1* was deleted in the SGA query strain (Y7092) by replacement with the *natMX* antibiotic resistance marker, which provides resistance to the drug nourseothricin (NAT). To construct the *ptr1Δ ptr3Δ* double mutant, *PDR3* was deleted in the *ptr1Δ* mutant by replacement with the *Kluyveromyces lactis URA3* autotrophic marker, which permits cells to grow on synthetic media lacking uracil. The *ptr1Δ*, *ptr3Δ*, and *snq2Δ* single or double mutants were constructed by replacing the wild-type gene with the *natMX*, *K. lactis URA3*, and *K. lactis LEU2* markers, respectively. The *natMX*, *Kl.URA3* and *Kl.LEU2* markers were amplified from plasmids using primers designed with 50 base pairs of sequence homologous to regions upstream and downstream of the genes. PCR amplicons were transformed into the appropriate strains using lithium acetate and polyethylene-glycol-based transformations. Deletion of the native gene and integration of the marker at the correct locus was confirmed using a series of PCR-based confirmations. Confirmation primers were designed specific to regions both flanking the integration site and internal to the inserted marker to interrogate both the full length of the inserted marker and the 5' and 3' boundaries.

The *MATα ptr1Δ::natMX ptr3Δ::Kl.URA3 snq2Δ::Kl.LEU2* (y13206) query strain carried the *can1Δ::STEpr-SP_his5* and *lypΔ* SGA reporters. *STEpr-SP_his5* is an auxotrophic marker that allows only *MATα* cells to grow in the absence of histidine, whereas the *can1Δ* and *lypΔ* deletions allow haploid cells to grow in the presence of the drugs canavanine and thialysine, respectively. The *MATα* query strain was crossed to an ordered array of *MATα xxxΔ::kanMX* deletion mutants and the resulting heterozygous diploids were transferred to media with reduced carbon and nitrogen to induce sporulation and the formation of haploid meiotic progeny. The resulting spores were transferred to synthetic media lacking histidine and containing canavanine and thialysine to select for the *MATα* meiotic progeny. Cells were then transferred to synthetic media lacking uracil and containing NAT to select for growth of cells carrying both the *ptr3Δ::Kl.URA3* and *ptr1Δ::natMX* deletions. Finally, these cells were transferred to synthetic media lacking uracil and leucine and containing G418 and NAT to select for the desired *ptr1Δ ptr3Δ snq2Δ xxxΔ* mutants.

Assessing compound hit rate of sensitized yeast strains. The chemical sensitivity of deletion mutants was assessed using a high-throughput chemical growth inhibition halo assay. After growing WT, *ptr1Δ ptr3Δ*, and *ptr1Δ ptr3Δ snq2Δ* mutant yeast strains overnight to saturation, cultures were standardized to an optical density at 600 nm (OD_{600}) = 4.0 and 2 mL was added to a 50-mL stock of 2% YP (10 g/L yeast extract, 20 g/L peptone) + 2% galactose + 1% agar (YPGal). Seeded plates were prepared by pouring 10 mL of culture into NUNC square plates and drying for 10 min to facilitate compound absorption. Robotic pinning with the BioTec ADS384 was used to transfer 0.2 μ L of each natural product to the seeded plates at a density of 88 compounds per plate; 440 diverse compounds (Supplementary Data Set 1) from the RIKEN NPDepo were evaluated in total. After incubating for 24 h at 30 °C, plates were imaged and the visible areas of growth inhibition were measured using JMicroVision (version 1.2.2. <http://www.jmicrovision.com>). A compound was deemed toxic if it generated an area of growth inhibition with a diameter greater than 1 mm. Thus, we assessed the number of compounds that perturbed growth (for example, compound hits) of the WT and the *ptr1Δ ptr3Δ*, and *ptr1Δ ptr3Δ snq2Δ* mutant strains.

The chemical sensitivities of the top drug-sensitive deletion mutants identified from the adapted assay were confirmed by growing deletion strains in the presence of the tested drug (34.4 μ M benomyl, 25 nM micafungin, or 1% DMSO) for 24 h and recording the resulting OD_{600} . Strains tested harbored deletions either in a wild-type background or in the drug-hypersensitive *ptr1Δ ptr3Δ snq2Δ* background. Values plotted are percentages calculated by dividing the OD_{600} measured after growth in DMSO by the OD_{600} measured after growth in the specific concentration of compound and multiplying by 100 (Fig. 1c,d). Y7092 was used as the WT control and the *ptr1Δ ptr3Δ snq2Δ* mutant was used as the drug hypersensitive control ($n = 3$ experimental replicates).

Defining the diagnostic gene set for optimized chemical-genetic screens. A diagnostic set of 310 genes was selected by combining the output from

two methods: a computational strategy and a manual selection. A set of 157 genes was selected by identifying functionally relevant genes using a computational approach called COMPRESS-GI⁵¹. Because genetic interaction profile similarity can be accurately measured using only a subset of the genome-wide profile, the COMPRESS-GI method selects genes to be included in a genetic-interaction (and chemical-genetic) profile to maximize the agreement between pairwise gene similarities computed from the compressed profile and gene co-annotation information from the Gene Ontology Consortium. Selection of such a subset of genes is useful for our chemical-genetic study, because the reduced chemical-genetic profile for each compound is directly compared with the corresponding reduced genetic-interaction profiles, generating accurate compound-gene similarities based on a small set of mutants. The COMPRESS-GI algorithm is described and evaluated in depth elsewhere⁵¹.

In addition to the 157 genes selected with the computational approach, we also manually selected 236 genes. The logic for the manual method was to pick any single member of the same pathway and/or complex because members of the same pathway/complex possess similar genetic interactions. Hence, picking one gene from each pathway/complex should be sufficient to cover the genetic network space associated with all the genes in that pathway/complex. We applied two-dimensional hierarchical clustering to cluster gene deletion mutants based on their genetic interaction profiles, and then manually selected strains that displayed rich genetic interaction profiles representative of each of the 17 functionally enriched clusters from the global genetic interaction profile similarity network¹¹) to generate a minimal subset of yeast deletion mutants that re-capitulated the majority of functional profiles observed in our reference map.

Both the COMPRESS-GI and manual gene selection methods were applied using a filtered, nonessential yeast genetic interaction data set¹² in which strains observed to exhibit extreme read counts in barcode sequence (top/bottom 10%) were removed. Furthermore, in cases where multiple different mutant alleles were available for the same gene, the allele with the highest number of genetic interactions (highest interaction degree) in its genetic interaction profile was chosen. We found 83 genes in common between the computational and manually derived lists, suggesting that the two methods had good agreement with respect to finding which genes were informative. The union of genes from the two selection methods comprised the initial diagnostic strain set (Supplementary Data Set 2).

Pilot experiments using this diagnostic set (Supplementary Data Set 2, diagnostic pool version 1) revealed a number of mutants that still exhibited abnormally high or low barcode counts in all experiments. These were removed to generate a collection of 310 strains for the final version of the diagnostic strain set (Supplementary Data Set 2, diagnostic pool version 2).

Optimization of signal detection and sequencing parameters. Initial optimizations were conducted using a preliminary diagnostic pool of 491 strains. This pool of deletion mutants was constructed by pinning frozen 96-well glycerol stocks of each strain onto Nunc Omni Tray plates containing YPD + G418 solid media and incubating for 2 d at 30 °C. Each plate was then flooded with 10 mL of YPD liquid media and a cell spreader was used to resuspend grown colonies. The resulting cell suspensions were transferred to a 50 mL conical tube where glycerol was added to a 15% final concentration. Finally, the pool was adjusted to a final concentration of 50 OD_{600} /mL by dilution or centrifugation and stored at -80 °C until required. To assay the mutant pool for drug hypersensitivity, cells were thawed, counted using a hemocytometer, and diluted to seven different final inoculum densities (3,727–58 cells/strain) in YP + 2% galactose in a 96-well flat-bottom plate. Cultures were then spiked with either 34.4 μ M benomyl, 25 nM micafungin, or a 1% DMSO control. After growing for 18, 24, or 48 h at 30 °C, cells from each well were harvested by centrifugation. Genomic DNA was purified from the harvested cells by resuspending in 125 μ L of zymolyase buffer (1 mg/mL) and using the QIAextractor (Qiagen) as per manufacturer's instructions, with a 100 μ L elution volume.

Barcodes were amplified from each of the wells using multiplex primers as described elsewhere³⁶ for 20, 25, or 30 cycles. Samples were gel purified from 2% agarose and assessed for quality using the Kapa Illumina qPCR kit. Samples were sequenced at a loading concentration of 10 pM on an Illumina HiSeq 2000

as a single uninterrupted read ('readthrough'). The 30-cycle samples were also sequenced using a 'separated read' strategy, where the barcodes were read in a first sequencing step, while the multiplex tags were read after a second priming step. Output from "read-through" and "separated read" runs were then compared. The signal-to-noise ratio was calculated by taking the mean CG score of the top 10 array genes divided by the s.d. of all array genes CG scores. This was done for each drug, PCR cycle, cell density and culture combination.

Multiplex tag design and 768-plex primer selection. We designed 1,000 10-bp multiplex tags such that (1) the Levenshtein distance between any two tags was greater than three, and (2) the tags were balanced in terms of nucleotide distribution. Condition (1) ensures that multiplex tags are maximally distinguishable even with a small number of sequencing errors whereas condition (2) ensures that the GC content and predicted melting point of all tags were within a small range. Because the space of multiplex tags is too large to exhaustively enumerate, we generated random multiplex tags and selected tags iteratively if both conditions were true. Primers containing the Illumina sequencing adaptor, common priming site for the UPTAG barcode, and 1,000 selected 10-bp multiplex tags were synthesized (Sigma), arrayed in 96-well plates. To assess amplification performance of the multiplex tags, we performed 1,000 identical pooled growth experiments on the diagnostic strain pool under control conditions (DMSO). Samples were processed as described above and sequenced on an Illumina MiSeq lane (1,000-plex). We used the count distribution to identify eight plates (768 multiplex tags) with the most uniform distribution of read counts (**Supplementary Fig. 13**), and discarded plates containing multiplex tags with highly divergent reads counts. These eight plates of multiplex tags with equivalent performance were used in all subsequent experiments (**Supplementary Data Set 3**).

To test the effects of multiplexing on the chemical genetic interaction signal, we selected a set of 768 compound conditions, including DMSO controls, known agents, and novel bioactive compounds from the RIKEN collection. For each assay we used the optimal pooled growth conditions defined above. We included a subset of compounds also screened in the Parsons *et al.* 2006 data set as controls at every plexing level (96, 192, 384, and 768)⁷. We dosed the pooled cells at a level that inhibited growth by 20–50% compared to the DMSO control. Genomic DNA extraction, PCR, sample prep, and sequencing were performed as described above.

Screening the NPDepo, NCI, NIH, and GSK collections. We performed our pooled growth assay with the diagnostic mutant collection under optimized conditions as described above. Excluding controls compounds, we performed two screens totaling 13,524 conditions representing 13,431 uniquely-named compounds. In the initial batch of compounds examined, we screened the first 9,840 members of the growing RIKEN NPDepo, and in the second batch, we screened six publicly available plated libraries: the NCI Natural Product (117 compounds), Approved Oncology (101), Structural Diversity (1,599), and Mechanistic Diversity (821) collections, the NIH Clinical Collection (720), and the GlaxoSmithKline kinase inhibitor collection (326). The NPDepo is maintained as 1 mg/mL stocks, and we screened it at a final concentration of 10 µg/mL, with the exception of a number of compounds that received additional lower dosing in a pilot experiment (**Supplementary Data Set 4**). All remaining collections were screened at 100 µM, except for the NCI Mechanistic Diversity set (10 µM; **Supplementary Data Set 4**). Selected compounds were re-screened at lower concentrations if the initial concentration resulted in severe growth inhibition. The diagnostic mutant pool was grown in 200 µL cultures in 96-well plates. Each plate had 88 test compounds, 4 control compounds, and 4 internal DMSO conditions (**Supplementary Fig. 14**). Each lane consisted of seven compound plates and one DMSO control plate, and every plate had three independent PCR replicates. For pairs of replicates of our control compounds, we measured Pearson correlation coefficients of 0.94, 0.95, 0.93, and 0.92 for our control compounds for Benomyl, Micafungin, MMS, and Bortezomib, respectively. Thus, three replicates were sufficient to ensure high-quality, quantitative chemical-genetic profiles. The primer set used to amplify each plate was shuffled for each replicate in such a way that each compound replicate would not use any single multiplex tag more than once. The primer set used to amplify the DMSO plate was different for each

lane. The control compounds give very distinct CG profiles and were used to ensure proper plate orientation at all steps of the process. Culture OD was measured at 0, 24, and 48 h, and growth at 24 h relative to the DMSO control was used as a measure of bioactivity.

Following growth, genomic DNA was extracted as described above. The genomic extractions for each plate were amplified in triplicate using three unique multiplex primer plates (three technical replicates). We used 768-plexing per lane, which means each sequencing lane contained PCR-amplified barcodes from eight 96-well plates. We ensured each of the multiplex primer plates were used to amplify the DMSO plates allowing us to detect and remedy any potential multiplex primer biases following sequencing. Following PCR, samples were pooled first by plate, then by lane. The 'per lane' samples were purified by 2% agarose gel and the product quantified by qPCR as described above. All samples were run at a loading concentration of 10 pM as single-end, 50 bp reads on an Illumina HiSeq 2000.

Description of compound collections. **RIKEN NPDepo.** The RIKEN Natural Products Depository (NPDepo) is a public depository of small molecules. Currently, the NPDepo chemical library contains 39,200 pure compounds, half of which are natural products and their derivatives⁵².

Each of the remaining collections are publicly available and can be requested at the sites listed below.

NIH-Clinical collection:

<https://commonfund.nih.gov/molecularlibraries/tools>

NCI-Structural diversity collection:

https://dtp.cancer.gov/organization/dscb/obtaining/available_plates.htm

NCI-Mechanistic diversity collection:

https://dtp.cancer.gov/organization/dscb/obtaining/available_plates.htm

NCI-Oncology collection:

https://dtp.cancer.gov/organization/dscb/obtaining/available_plates.htm

NCI-Natural products collection:

https://dtp.cancer.gov/organization/dscb/obtaining/available_plates.htm

GSK-Kinase inhibitor collection:

<https://www.ebi.ac.uk/chembl/db/extra/PKIS/>

Computing molecular descriptors for all screened compounds. SMILES and InChI string representations of all molecules were generated using the OpenBabel cheminformatics toolkit⁵³ (<http://openbabel.org>) and its python wrapper, pybel⁵⁴. All molecular descriptors (column L through the last column) were calculated using PaDEL-Descriptor⁵⁵, a wrapper for the Chemistry Development Kit cheminformatics toolkit⁵⁶.

Predicting compounds' modes of action based on chemical-genetic and genetic-interaction profiles. Full descriptions of the methods for scoring chemical-genetic interactions from next-generation sequencing data and predicting targeted biological processes via integration of genetic and chemical genetic interaction profiles are presented in the **Supplementary Note**.

To assess the performance of predictions, we identified known compounds with described modes of action present in our high-confidence prediction set ("gold standard compounds"). If the predicted process was functionally related to the known mode of action, we considered this a successful prediction (**Supplementary Table 3**).

Characterizing the contribution of strains with high and low chemical-genetic interaction degree to process-level target prediction. We characterized the contribution of the highest- and lowest-degree strains to process-level predictions, this time by removing the 15% highest- or lowest-degree strains before predicting process-level targets. The degree of a strain was defined as the number of interactions with an absolute CG score ≥ 2.5 it possessed across the RIKEN subset of compound-derived chemical-genetic interaction profiles (no DMSO or resampled profiles). After removing 40 of the highest-degree or 41 of the lowest-degree strains (out of the 275 strains) that overlapped with the *S. cerevisiae* genetic interaction network array strains (**Supplementary Data Set 9**), process-level targets were predicted as described in 'Predicting compounds' modes of action based on chemical-genetic and genetic-interaction profiles' and 'Assessing the false discovery rate of process target predictions'

in **Supplementary Note**. Comparisons regarding the number and identity of discovered compounds, and the identity of their predictions, were performed to determine the roles that high and low chemical-genetic interaction degree strains played in predicting process-level targets.

While the removal of low-degree strains had little effect on the identity of discovered compounds and their predictions, the removal of high-degree strains had noticeable effects. The ‘no-low-degree’ profiles led to discovery of 927 compounds with high-confidence GO biological process predictions, 794 of which matched the original RIKEN ‘all-strain’ discovered compounds (94% of the 848 original RIKEN high-confidence set, or HCS) (**Supplementary Data Set 9**). In contrast, the ‘no-high-degree’ profiles led to the discovery of only 667 compounds with high-confidence GO biological process predictions, most of which overlapped with the RIKEN HCS (537 compounds, or 63% of the RIKEN HCS). In addition, the predictions derived from ‘no-low-degree’ profiles tended to match the predictions of in the RIKEN HCS (602/794, or 76%, of ‘all-/no-low-degree’ compounds shared predictions with Jaccard ≥ 0.25), while the predictions derived from ‘no-high-degree’ profiles were less consistent (168/667, or 31%, of ‘all/no-high-degree’ compounds shared predictions with Jaccard ≥ 0.25).

The importance of high-degree strains to bioprocess-level predictions was further confirmed by examining the identities of the predicted processes. Although removing high-degree strains does not destroy the performance of bioprocess-level predictions, it does substantially change the distribution of the most frequently predicted bioprocesses and reduce prediction accuracy for some well-characterized compounds. After removing high-degree strains, the top predicted bioprocess by far was “spindle assembly,” followed by other microtubule and cell-cycle-related processes, and, finally, bioprocesses related to localization, pH and ATP, glycosylation, and DNA damage and repair (**Supplementary Data Set 9**). For three well-characterized compounds, the removal of high-degree strains substantially reduced prediction specificity for tunicamycin, altered predictions of rank 3 and below for benomyl, and left the predictions for MMS essentially unchanged (**Supplementary Data Set 9**). In contrast, removing low-degree strains had little effect on either the distribution of process-level predictions in the high-confidence set or the highest-confidence predictions for benomyl, MMS, and tunicamycin.

Characterizing the respective contribution of negative and positive interactions to process-level target prediction. Using the RIKEN NPDepo high-confidence set of compounds, we characterized the contribution of positive and negative chemical-genetic interactions to our process-level predictions. First, chemical-genetic interaction profiles containing either only positive or only negative interaction scores were generated. Process-level targets were then predicted using these ‘positive-only’ or ‘negative-only’ profiles as described in ‘Predicting compounds’ modes of action based on chemical-genetic and genetic interaction profiles’ and ‘Assessing the false discovery rate of process target predictions’ in **Supplementary Note**. We then compared the number and identity of the compounds discovered, and the identity of their predictions, between ‘positive-only’, ‘negative-only’, and ‘all-interaction’ prediction sets to determine which side(s) of the chemical-genetics interaction profiles were important for predicting perturbed processes.

Two schemes were employed to generate the ‘positive-only’ and ‘negative-only’ chemical-genetic interaction profiles and their subsequent process-level predictions. Scheme 1 profiles showed how all negative and all positive interaction scores contribute to process-level predictions, and scheme 2 profiles accounted for biases that could have occurred because of differences in the number of positive vs. negative interactions in the scheme 1 profiles. To generate ‘negative-only’ profiles under scheme 1, the positive scores in all compounds, DMSO control profiles, and resampled profiles were set to zero; conversely, ‘positive-only’ profiles under this scheme were generated by setting all negative scores to zero. To generate the ‘positive-only’ and ‘negative-only’ profiles under scheme 2, an equal number of scores with absolute value ≥ 1 were selected from the extreme positive or negative ends, respectively, for each compound, DMSO, and resampled profile.

‘Negative-only’ and ‘positive-only’ chemical-genetic interaction profiles led to the identification of a substantially different sets of ‘high-confidence’ compounds (at least one prediction with FDR $\leq 25\%$), with the

‘negative-only’ profiles reproducing the ‘all-interactions’ high-confidence set much better than did the ‘positive-only’ profiles. Both high-confidence sets derived from ‘negative-only’ profiles from scheme 1 (all scores) and scheme 2 (equal number of positive vs. negative scores) possessed roughly the same number and identity of compounds in comparison to the ‘all-interaction’ high-confidence set (**Supplementary Data Set 10**). Specifically, 85% (723/848) and 81% (689/848) of the high-confidence compounds identified using all interactions were discovered using scheme 1 ‘negative-only’ profiles (‘negative-all/all’ comparison) and scheme 2 ‘negative-only’ profiles (‘negative-equal/all’ comparison), respectively. Whereas the high-confidence set derived from scheme 1 ‘positive-only’ profiles was similar in size to the ‘all-interactions’ high-confidence set, the compounds in both scheme 1 and scheme 2 ‘positive-only’ high-confidence sets had much lower overlap with the ‘all-interactions’ high-confidence set (345/848, or 41%—‘positive-all/all’ comparison, and 183/848, or 22%—‘positive-equal/all’ comparison, respectively).

In addition to driving the discovery of the same compounds that were in the ‘all-interactions’ high-confidence set, negative chemical-genetic interactions also drove the discovery of the same predictions for these compounds. For example, 68% (494/723) of the ‘negative-all/all’ co-identified compounds and 47% (326/689) of the ‘negative-equal/all’ co-identified compounds had a Jaccard coefficient of ≥ 0.25 for their predictions. In contrast, only 17% (58/345) of the ‘all/positive-all’ and 3% (6/183) of the ‘all/positive-equal’ co-identified compounds met this criterion for the similarity of their predictions, suggesting that even for compounds for which predictions were made, the predicted modes of action were largely different. From this evidence, negative chemical-genetic interactions are clearly the primary driver of genetic-interaction-based target predictions.

In addition, two lines of evidence suggest that the predictions made using only positive chemical-genetic interactions are of lower quality than those derived from all or only negative interactions. First, we observed that the predictions from positive chemical-genetic interactions were overwhelmingly biased toward GO terms related to RNA splicing/processing and cell cycle/mitosis, whereas those from all or only negative interactions were more diverse (GO terms related to cellular localization, chromatin organization and transcription, cell wall, vesicle-mediated transport, pH regulation, protein degradation, microtubules and cytoskeleton, etc., in addition to cell cycle/mitosis) (**Supplementary Data Set 10**). Second, we observed that in the set of predictions derived from only positive interactions, three well-characterized compounds (benomyl, MMS, and tunicamycin), whose known mechanisms of action are well captured by process-level predictions based on either all or only negative interactions, both (1) failed to make the high-confidence compound list and (2) did not show predictions consistent with known mechanisms (**Supplementary Data Set 10**).

Visualizing the relationship between compound bioactivity and inclusion into the high-confidence set. We assessed the fraction of compounds in the high-confidence set as a function of bioactivity, which can also be thought of as the probability that a compound will be in the high-confidence set given its bioactivity. The bioactivity (percent growth compared to DMSO) and high-confidence-set status (true/false, respectively, set to 1/0 for analysis) for each compound were extracted from **Supplementary Data Set 4**. A loess curve was then fit through the 1/0 high-confidence status values with respect to the bioactivity values, using a span of 0.1 and least-squares fitting with a polynomial degree of 2. The curve on the plot was drawn at points 2.5 units apart, starting at the smallest observed bioactivity value (**Supplementary Fig. 6**).

Determining functional distributions of compound collections. *Generating the background set of chemical-genetic profiles.* To account for biases in the distribution of process predictions introduced by our discovery pipeline, we generated a set of ‘background’ chemical-genetic profiles. Each background profile was a high-signal GI profile with noise added based on the variance of each strain across all GI profiles (Gaussian, $\mu = 0$, $\sigma = 2 \times \sigma_{\text{strain}}$). Each of these 4,515 profiles (3 background profiles for each of 1,505 GI profiles) simulated a compound that targets one gene. This enabled the estimation of any functional biases introduced by our GI-based discovery pipeline.

Computing distributions of process predictions for each compound class. We calculated the proportion of each compound class that was predicted to each

process term. (**Supplementary Data Set 20**). Those proportions were then compared to the proportion of the background profiles predicted to each process using a proportion test in R (**Supplementary Data Set 21**). To sort from the most significant enrichment to the most significant depletion compared to the background, *P* values from the proportion test were modified such that *P* values from proportions greater than the background ranged from 0 to 1, and *P* values from proportions smaller than the background ranged from 2 to 1. Using a rank-sum analysis with the modified *P* values as the input, we determined, for each class, whether processes that mapped to each functional neighborhood were predicted more or less frequently than in the background set. Rank-sum *P* values were Bonferroni corrected and visualized as a heatmap (**Fig. 4b**).

Compound diversity sets for functional neighborhoods. We assigned all the compounds associated with a specific functional neighborhood to a single cluster and split up the cluster recursively to form clusters of more similar compounds. At any recursive step, we determined the cluster with the lowest average within-cluster chemical-genetic profile similarity and divided the cluster into two new clusters using K-means clustering. We stopped generating new clusters right before our algorithm would generate at least two individual clusters, exceeding our predefined limit for the maximum average between-cluster chemical-genetic profile similarity (cosine similarity of 0.3). We repeated the algorithm 1,000 times for each neighborhood and selected, from each cluster, the compound with the strongest prediction as a candidate for our diversity set. We finally sorted all our candidates across all the repetitions from the most to the least frequently occurring. To define the compound diversity set, we selected from this ranked list as many top candidates as were needed to cover all the clusters in at least 50% of the repetitions.

Comparison with other chemical-genetic data sets. An independent set of whole-genome chemical-genetic screens have been performed previously by Lee *et al.* and Hoepfner *et al.*^{8,17}. These two studies interrogated 3,239 and 2,923 compounds, respectively, and they were performed using both a heterozygous and homozygous diploid deletion mutant profiling platform. The homozygous diploid deletion mutant profiling platform is comparable to the chemical-genetic analysis we carried out with haploid deletion mutants. Our study shares 145 compounds in common with the Lee *et al.* study and 31 compounds in common with the Hoepfner *et al.* study. Specifically, all three studies possessed an overlap of nine compounds.

Comparisons were made between our chemical-genetic interaction scores and the Hoepfner *et al.* median absolute deviation logarithmic scores, and the Lee *et al.* fitness defect scores (multiplied by -1), such that the chemical-genetic interaction profiles were restricted to the 277 genes common between the three studies. For the nine shared compounds (**Supplementary Table 1**), our study shows an average Pearson correlation coefficient (PCC) of 0.29 with Lee *et al.*, and of 0.38 with Hoepfner *et al.*, whereas Lee *et al.* and Hoepfner *et al.* show a PCC of 0.22. Thus, our study shows significant agreement with both the Lee *et al.* study ($P = 5 \times 10^{-7}$) and the Hoepfner *et al.* study ($P = < 1 \times 10^{-8}$).

We also compared the members of the compound diversity sets derived from our RIKEN and Clinical screens to the major chemical-genetic signatures defined in Lee *et al.*, and found favorable overlap of the functional space occupied by compounds from both studies. After computing PCC between each diversity set compound and each compound from Lee *et al.* that was annotated to a major signature, we observed that all 45 major Lee *et al.* signatures contained at least one compound that was significantly similar to a compound in both diversity sets (PCC > 0.2; one-sided test; *P* values obtained by shuffling the profile gene labels 10,000 times followed by Benjamini–Hochberg correction; FDR < 0.05) and that most of the compounds in the RIKEN and clinical diversity sets contributed to this overlap (123/130 unique RIKEN and 187/214 Clinical compounds; **Supplementary Fig. 15a**). When applying a more stringent PCC threshold (PCC > 0.4), only 18 and 12 (out of 45) major signatures from Lee *et al.* are covered by 32 and 39 compounds from the RIKEN and Clinical diversity sets, respectively.

In addition, we mapped the Lee *et al.* major signatures to our bioprocesses and found that many of these mappings agree functionally (**Supplementary Fig. 15b**). After computing PCC between the profiles of each high-confidence

compound and each compound from Lee *et al.* that was annotated to a major signature, we annotated each correlation > 0.3 to a major signature/bioprocess pair (the bioprocess annotation for each high-confidence compound was based on its best process prediction). For each major signature/bioprocess pair, we then counted the number of unique Lee *et al.* and high-confidence compounds, respectively, that contributed to these correlations. We normalized these counts by the size of their respective major signature or bioprocess and multiplied the resulting fractions together to derive a confidence score that deemphasizes major signature/bioprocess pairs for which a very small number of compounds annotated to the major signature (or bioprocess) is responsible for most of the correlations to the compounds in the bioprocess (or major signature). A table that maps each Lee *et al.* major signature to its most confident bioprocess is provided (**Supplementary Data Set 22**), as is a table that maps each Lee *et al.* signature to any bioprocess with which it shared at least one profile correlation > 0.3 (**Supplementary Data Set 22**). Both tables are sorted by confidence in descending order. Agreement between the Lee *et al.* major signatures and our bioprocess annotations was encouraging; specifically, Golgi (Lee *et al.*) mapped to Vesicle traffic (this study), ubiquinone biosynthesis and proteasome (Lee *et al.*) to Protein Degradation (this study), ergosterol depletion effects on membrane (Lee *et al.*) to Metabolism and Fatty Acid Biosynthesis (this study), and DNA damage response (Lee *et al.*) to DNA Replication and Repair (this study). Overall 43/45 major chemical-genetic signatures possessed at least one compound with PCC > 0.3 to a compound in our study and therefore could be mapped to a bioprocess; however, mappings derived from a very small number of compounds in either member of the pair should be interpreted with more caution.

Identifying structural motifs contributing to functional enrichments. To identify structural motifs that drove specific functional neighborhood enrichments, we performed discriminative molecular substructure mining on the RIKEN HCS set of compounds using the MoSS tool⁵⁷. Using the proportion of each compound class that was predicted to each process term (see ‘Computing distributions of process predictions for each compound class’), we selected only process terms that had a significantly higher proportion of predictions in at least one compound class versus the GI background (proportion test in R; Bonferroni corrected). Then, for each process term, we identified substructures that occurred at least twice as frequently in compounds with high-confidence predictions to that process term (the ‘active’ set) versus compounds that did not have high-confidence predictions to that term (the ‘inactive’ set). This discriminative mining was performed twice per process term: once by drawing the inactive set of compounds from all screened compounds in the RIKEN NPDepo, and once by drawing the inactive set from all NPDepo compounds in the HCS. By selecting the minimum of these two enrichments, we sought to control for bias in the distribution of substructures in the inactive compounds. The information about the substructures and their enrichments was compiled across all experiments. The final output is a table of substructures that show enrichment for a particular functional category (**Supplementary Data Set 15**).

Localization enrichments. We sought to determine if the compounds in particular collections exhibited bias in the localization of their targets. Using the proportion of each compound class that was predicted to each process term (see ‘Computing distributions of process predictions for each compound class’), we selected process terms that had significantly higher (enriched) and lower (depleted) proportions of predictions versus the GI background (proportion test in R; Bonferroni corrected). For each compound collection, two gene lists were assembled, each representing the union of the genes annotated to either enriched or depleted ($p_{\text{bonf}} \leq 0.05$) process terms.

A hypergeometric test was performed to determine which of these gene lists were enriched for genes annotated to specific cellular components. *P* values were Bonferroni-corrected. Gene annotations to cellular compartments were obtained from refs. 58 and 59, and the yeast GO slim cellular compartment annotations (<http://www.yeastgenome.org/>). The background set of genes for all hypergeometric tests was the set of 1,499 query genes with GO process annotations from the high-degree genetic interaction data set.

Flow cytometry based global validations of targeted processes. Sixty-seven compounds with process target predictions mapping to G1 phase arrest, S phase arrest, or G2 phase arrest flow cytometry phenotypes (based on ref. 35) were selected from the high-confidence set. Compounds that ultimately mapped to multiple cell cycle phenotypes via their process target predictions were removed from consideration. For each cell cycle phenotype, the 50 compounds with the highest overlap of (1) gene targets driving the process prediction that mapped to the phenotype and (2) the genes directly annotated to the phenotype³⁵ were selected. Compounds were then manually selected from these lists based on their bioactivity, as compounds with higher bioactivity were assumed more likely to induce a cell cycle phenotype.

Cultures of the control strain (y13206) were grown to early log phase (0.4 OD) in YPGal (1% yeast extract, 2% peptone, 2% galactose). 250 μ L per well of the starting culture was aliquoted into a 96-well block. The cultures were treated with 10 μ g/mL of each compound and incubated at 30 °C for 2–3 h. We included the compounds hydroxyurea, MMS, nocodazole, and tunicamycin as controls known to arrest cell cycle in G1, S, G2 and post-G2 respectively. From each culture, 200 μ L was transferred into a new 96 well plate, pelleted at 2,000 r.p.m. for 5 min. Pellets were resuspended in 20 μ L of 50 mM Tris–Cl (pH 8.0), 50 mM EDTA buffer. 160 μ L of cold 99% EtOH was added to the wells. Cells were pelleted at 4,000 r.p.m. for 2 min at RT, resuspended in RNase A solution (50 mM Tris–Cl pH 8.0, 0.4 mg/mL RNase A), and incubated for 2 h at 37 °C. Cells were pelleted at 4,000 r.p.m. for 2 min at RT, and 50 μ L of proteinase K solution was added (50 mM Tris–Cl pH 7.2, 200 mM NaCl, 78 mM MgCl₂, filter sterilized). The cells were then incubated for 50–60 min at 50 °C. Cells were pelleted at 4,000 r.p.m. for 2 min at RT, and resuspended in 55 μ L of FACS buffer (200 mM Tris–Cl pH 7.5, 200 mM NaCl, 78 mM MgCl₂, filter sterilized). In a new 96 well plate, 180 μ L of SYBR Green solution (2X SYBR Green, 50 mM Tris–Cl pH 7.2) was added to each well. 20 μ L of fixed cells from the previous step was added. The plate was then processed via high-throughput flow cytometry as described in ref. 35. The voltage of the green channel was adjusted so that on the linear scale the 1C peak and the 2C peak were well spaced, the 1C peak was away from the vertical axis. The FSC-A vs FL1-A was used to gate out aggregates and dead cells. The final histograms have FL1-A on the x-axis (area of the green channel).

Cell cycle phenotypes were called by drawing thresholds based on 46 control DMSO profiles, on either the percent of cells in S phase (%S) or the ratio between the percentages of cells in G1 (1C peak) vs. G2 (2C peak) phase (G1/G2 ratio). Specifically, the mean and s.d. were computed for both the %S and the G1/G2 ratio in the DMSO control samples. These values were used to convert the corresponding values from the treatment compounds into z-scores. A phenotype was called if the z-scores of both replicates passed the appropriate z-score threshold of either 1.5 or –1.5. The specific thresholds for phenotypes calls were as follows: a 1C phenotype was called if G1/G2 ratio > 1.196; a 2C phenotype was called if G1/G2 ratio < 0.809; and an S phenotype was called if %S > 19.5%.

Enrichments and *P* values were computed empirically by shuffling the phenotypes associated with the compounds and counting the number of cell cycle phenotypes associated with each prediction in the shuffled data (100,000 randomizations). Compound identities were preserved during the randomization, such that both replicates of a compound were associated with the same cell cycle phenotype prediction after each randomization. Enrichments were computed by dividing the number of calls observed from the real data by the average expected number of calls for each combination of predicted and observed phenotype (averaged over all compound-predicted phenotype randomizations). In a similar fashion, empirical *P* values were computed for each combination of predicted and observed phenotype by counting the fraction of randomizations that produced the same or larger number of calls.

Multi-parameter validation of cell wall targeting compounds. To test for compound-induced cell leakage, an adenylate kinase (AK) assay was used. An overnight culture of the drug hypersensitive yeast strain (y13206) in log phase was harvested and washed twice with fresh YPGal medium. The final pellet was resuspended in 1 mL fresh YPGal. Fifty microliters of cell suspension (~1 \times 10⁶ cells), 1% DMSO, 30 mM hydroxyurea, 20 μ g/mL echinocandin B, 40 μ g/mL NPD5925, or 10 μ g/mL of other test compounds were added in

individual wells of 96-well culture plate containing YPGal medium to a final volume of 100 μ L, mixed by pipetting and incubated at 25 °C for 4 h (*n* = 3 experimental replicates). The plate was equilibrated to room temperature for 30 min and the contents were transferred into a luminescence compatible 96-well white-walled plate. Next, 100 μ L of ToxiLight AK reagent (Lonza) was added to each well and incubated at room temperature for 30 min, and luminescence was measured with a Wallace ARVO SX 1420 Multilabel Counter (PerkinElmer Life Sciences). Hit compounds resulted in more than 90,000 units. Cells were stained with the glucan stain aniline blue and the chitin stain calcofluor white as described previously³⁶, and hits assessed by irregular glucan or chitin staining detected by eye. Treated cells were analyzed by high-dimensional morphometric analysis (CalMorph) as described previously (*n* \geq 2)⁶⁰.

Zymolyase sensitivity assay. Yeast cells (y13206) were grown in YPGal until log phase (~4 \times 10⁷ cells/mL), and 50 μ L of aliquot was transferred into fresh 150 μ L YPGal containing test compounds in 96-well microtiter plate (10 or 40 μ g/mL for test compounds, as for controls: 2.5 μ g/ml for echinocandin B, 30 mM for hydroxyurea, 1% for DMSO). The cell-containing plate was incubated at 25 °C for 4 h with shaking. After incubation, cells were washed twice with 10 mM Tris–HCl (pH 7.5), and resuspended to zymolyase solution (0.94 mg/mL of Zymolyase 100T (Seikagaku) in 10 mM Tris–HCl (pH 7.5)). Cell suspensions were incubated at 30 °C, and OD₆₀₀ values were measured for 1 h after the addition of zymolyase with plate reader (SPECTRAMax plus384, Molecular Devices). In each sample, OD₆₀₀ values were standardized at time 0 to equal 1 (or 100%).

Cell cycle analysis of NPD5925. Y13206 cells were grown to mid-log phase in YPD, and a sample of this asynchronous population was saved for later analysis. The cells were treated with α -factor and incubated for 2.5 h at 30 °C, and a sample of the α -factor-arrested population was saved for later analysis. Pronase and test compounds were added to the remaining arrested population. We tested DMSO (2%), hydroxyurea (0.2 M), MMS (0.03%), and NPD5925 (20 μ g/mL). The treated cells were incubated for 1 h and then prepared and analyzed via flow cytometry as described above.

Tubulin inhibition assay and assessing predictive power. We carried out *in vitro* tubulin polymerization assays using the cytoskeleton fluorescent-based porcine tubulin polymerization assay (Cytoskeleton, Inc.) following manufacturer specifications. We used 10 μ g/mL of test compound for each assay. We tested the control compounds nocodazole, paclitaxel, and the predicted tubulin targeted compound NPD2784 versus a DMSO solvent control.

Identifying compounds with multiple, unique mechanisms of action. We devised an algorithm to prioritize compounds from the RIKEN HCS whose chemical genetic (CG) interaction profiles appeared to be a combination of multiple, diverse genetic interaction (GI) profiles, indicating that they exert their effects via multiple, unique mechanisms of action. For a compound, we first constructed profiles reflecting the mean contribution of each strain in its CG profile to each of its process target (PT) predictions. Then, the initial cluster of ‘mean contribution profiles’ was seeded with the profile from the highest-confidence PT prediction. To complete the clustering, the mean contribution profiles from progressively lower-confidence PT predictions were either added to an existing cluster (if they possessed a Pearson correlation coefficient of \geq 0.5 with a profile in that cluster) or used to seed a new cluster. Compounds were prioritized if they possessed two clusters of mean contribution profiles with very low average similarity between them, suggesting that two distinct signals in the GI network contributed to the signal observed in their CG profiles. A set of contribution profiles was generated for a compound and one of its PT predictions by taking the element-wise product of the compound’s CG profile and the L₂-normalized GI profile of each gene that drove the PT prediction (genes with genetic target score \geq 2 and were annotated to the PT, which are shown in columns ‘driver_common’ and ‘driver_score’ in **Supplementary Data Set 8**. The ‘mean contribution profile’ for one compound and PT prediction was calculated as the strain-wise mean across all of the contribution profiles

associated with that compound and one PT prediction. GI profiles were from the set of high-signal genetic interaction profiles. To identify instances where a dual process prediction could potentially be a result of the compound instead targeting a single, pleiotropic gene, the mean contribution profile for the top bioprocess predictions for each compound were also separately correlated with all possible genes. Candidate dual targeting compounds for which a single gene showed significant similarity to both contribution profiles were considered not to have evidence for multiple modes of action.

Staining of cells with NPD5925. Log phase yeast cells (y13206) were fixed with 3.7% formaldehyde solution. The fixed-cell suspension was centrifuged to make cells a pellet, and the pellet was mixed with the same volume of NPD5925 (1 mg/mL) and incubated at 25 °C for 30 min. Cells were washed twice with phosphate-buffered saline (PBS), and a small cell aliquot was mixed with mounting solution (90% glycerol, 9.975% PBS, 0.025% 0.1 N NaOH) containing *p*-phenylenediamine (1 mg/mL) and 4′6-diamidino-2-phenylindole (DAPI, 0.7 mg/mL). A prepared specimen was observed by fluorescent microscope (Axio Imager M1, Carl Zeiss) with regular rhodamine or DAPI filter sets (Carl Zeiss). An intensity profile was extracted from cell images by ImageJ (<http://imagej.nih.gov/ij/>).

Code availability. All code used to generate these data are freely available via <http://github.com/csbio/>.

Data availability. We have established a database that hosts all the barcode sequence data at <http://mosaic.cs.umn.edu/>. All high-confidence chemical-genetic data and associated compound information has been

deposited to PubChem (Data Source ID <https://pubchem.ncbi.nlm.nih.gov/source/15567>). All data generated or analyzed during this study are included in this published article (and its supplementary information files) or are available from the corresponding author on reasonable request.

51. Deshpande, R. *et al.* Efficient strategies for screening large-scale genetic interaction networks. Preprint at <http://www.biorxiv.org/content/early/2017/07/05/159632> (2017).
52. Kato, N., Takahashi, S., Nogawa, T., Saito, T. & Osada, H. Construction of a microbial natural product library for chemical biology studies. *Curr. Opin. Chem. Biol.* **16**, 101–108 (2012).
53. O’Boyle, N.M. *et al.* Open Babel: An open chemical toolbox. *J. Cheminform.* **3**, 33 (2011).
54. O’Boyle, N.M., Morley, C. & Hutchison, G.R. Pybel: a Python wrapper for the OpenBabel cheminformatics toolkit. *Chem. Cent. J.* **2**, 5 (2008).
55. Yap, C.W. PaDEL-descriptor: an open source software to calculate molecular descriptors and fingerprints. *J. Comput. Chem.* **32**, 1466–1474 (2011).
56. Steinbeck, C. *et al.* The Chemistry Development Kit (CDK): an open-source Java library for chemo- and bioinformatics. *J. Chem. Inf. Comput. Sci.* **43**, 493–500 (2003).
57. Borgelt, C., Meinl, T. & Berthold, M. MoSS: A program for molecular substructure mining. In Proc. 1st International Workshop on Open Source Data Mining: Frequent Pattern Mining Implementations 6–15 (ACM, 2005).
58. Huh, W.-K. *et al.* Global analysis of protein localization in budding yeast. *Nature* **425**, 686–691 (2003).
59. Koh, J.L.Y. *et al.* CYCLOPs: A comprehensive database constructed from automated analysis of protein abundance and subcellular localization patterns in *Saccharomyces cerevisiae*. *G3 (Bethesda)* **5**, 1223–1232 (2015).
60. Ohya, Y. *et al.* High-dimensional and large-scale phenotyping of yeast mutants. *Proc. Natl. Acad. Sci. USA* **102**, 19015–19020 (2005).

ERRATA

Functional annotation of chemical libraries across diverse biological processes

Jeff S Piotrowski, Sheena C Li, Raamesh Deshpande, Scott W Simpkins, Justin Nelson, Yoko Yashiroda, Jacqueline M Barber, Hamid Safizadeh, Erin Wilson, Hiroki Okada, Abraham A Gebre, Karen Kubo, Nikko P Torres, Marissa A LeBlanc, Kerry Andrusiak, Reika Okamoto, Mami Yoshimura, Eva DeRango-Adem, Jolanda van Leeuwen, Katsuhiko Shirahige, Anastasia Baryshnikova, Grant W Brown, Hiroyuki Hirano, Michael Costanzo, Brenda Andrews, Yoshikazu Ohya, Hiroyuki Osada, Minoru Yoshida, Chad L Myers & Charles Boone

Nat. Chem. Biol.; doi:10.1038/nchembio.2436; corrected online 7 August 2017

In the version of this article initially published online, there were several typographical errors introducing scientific inaccuracies. In Figure 5a, the compound name NPE1136 was incorrectly written NPD1136. In the Discussion, the number of strains tested, 5,000, was incorrectly given as ~4,900. In the Online Methods, several strain descriptions in the sections “Constructing a genome-wide drug sensitive yeast deletion correction” and “Assessing compound hit rate of sensitized yeast strains” were incorrect or unclear (in particular, the *MATa xxxΔ:kanMX* yeast strain was indicated as *MA TaxxxΔ:kanMX*); the unit mL was given in place of the correct μL in several places in the sections “Multi-parameter validation of cell wall targeting compounds” and “Zymolyase sensitivity assay”; references 14 and 15 were cited instead of references 8 and 17 in the section “Comparison with other chemical-genetic data sets section”; and the list of molecular descriptors calculated using PaDEL-Descriptor in the section “Computing molecular descriptors for all screened compounds” should have started with column L, not J. These errors have been corrected in all versions of the article.